



**HAL**  
open science

## Sensitivity analysis of non-local damage in soft biological tissues

Di Zuo, Stéphane Avril, Chunjiang Ran, Haitian Yang, S. Jamaledin Mousavi, Klaus Hackl, Yiqian He

► **To cite this version:**

Di Zuo, Stéphane Avril, Chunjiang Ran, Haitian Yang, S. Jamaledin Mousavi, et al.. Sensitivity analysis of non-local damage in soft biological tissues. *International Journal for Numerical Methods in Biomedical Engineering*, In press, 10.1002/cnm.3427 . hal-03139932

**HAL Id: hal-03139932**

**<https://hal.science/hal-03139932>**

Submitted on 12 Feb 2021

**HAL** is a multi-disciplinary open access archive for the deposit and dissemination of scientific research documents, whether they are published or not. The documents may come from teaching and research institutions in France or abroad, or from public or private research centers.

L'archive ouverte pluridisciplinaire **HAL**, est destinée au dépôt et à la diffusion de documents scientifiques de niveau recherche, publiés ou non, émanant des établissements d'enseignement et de recherche français ou étrangers, des laboratoires publics ou privés.

# Sensitivity analysis of non-local damage in soft biological tissues

Di Zuo<sup>a</sup>, Stéphane Avril<sup>b</sup>, Chunjiang Ran<sup>a</sup>, Haitian Yang<sup>a</sup>, S. Jamaledin Mousavi<sup>b</sup>, Klaus Hackl<sup>c</sup>, Yiqian He<sup>a,d,\*</sup>

<sup>a</sup>*State Key Lab of Structural Analysis for Industrial Equipment, Department of Engineering Mechanics, Dalian University of Technology, Dalian 116024, P.R. China*

<sup>b</sup>*Mines Saint-Étienne, University Lyon, INSERM, U1059 Sainbiose, Centre CIS, Saint-Étienne F-42023, France*

<sup>c</sup>*Institute of Mechanics of Materials, Ruhr-Universität Bochum, Bochum D-44801, Germany*

<sup>d</sup>*Key Laboratory of Biorheological and Technology of Ministry of Education, Chongqing University, Chongqing 400030, P. R. China*

---

## Abstract

Computational modeling can provide insight into understanding the damage mechanisms of soft biological tissues. Our gradient-enhanced damage model presented in a previous publication has shown advantages in considering the internal length scales and in satisfying mesh independence for simulating damage, growth and remodeling processes. Performing sensitivity analyses for this model is an essential step towards applications in which it is necessary to handle the uncertainty caused by patient-specific data. [In this paper, a numerical analysis approach is developed by integrating two existing methods, i.e. the gradient-enhanced damage model and the surrogate model-based probability analysis, to address this need. To increase the computational efficiency of the Monte Carlo method in uncertainty propagation for the nonlinear hyperelastic damage analysis,](#) the surrogate model based on Legendre polynomial series is employed to replace the direct FEM solutions, and the sparse grid collocation method (SGCM) is adopted for setting the collocation points to further reduce the computational cost in training the surrogate model. The effectiveness of the proposed approach is illustrated by two numerical examples, including an application to the clinical problem of dilatation of the artery.

*Keywords:* Nonlocal damage, Uncertainty analysis, Soft tissues, Surrogate model, Computational efficiency

---

## 1. Introduction

Understanding the damage mechanism of soft biological tissues is critical to the characterization of tissue injuries [1, 2, 3, 4]. For instance, in the treatment of cardiovascular diseases, the focus is often on the potential risk of tissue rupture, which is mainly caused by soft tissue damage, such as atherosclerotic plaques or aneurysms [5]. The damage analyses

---

\*Corresponding author: heyiqian@dlut.edu.cn

6 of the tendons, which are important load-bearing structures and are frequently injured in  
7 both sports and work, are also important in understanding the underlying mechanisms and  
8 are helpful for treatment [6].

9 The damage modeling of soft biological tissues and its numerical computation has been a  
10 topic of intense research. Holzapfel et al. [7], Gasser [8] and Li [9] comprehensively reviewed  
11 the computational models for the damage of soft biological tissues. The developed damage  
12 models can be divided into three approaches [9]: (1) models based on continuum damage  
13 mechanics, (2) models based on the theory of pseudo-elasticity, and (3) the softening hyper-  
14 elasticity approach. [Among the continuum damage models, a gradient-enhanced non-local  
15 damage model was proposed by Dimitrijevic and Hackl \[10, 11\]](#), and a nonlocal continuum  
16 healing model that combines the gradient-enhanced damage model and a temporally homog-  
17 enized growth and remodeling model was originally presented in our previous works [12, 13].  
18 This model has the following advantages: (1) good mesh independence is achieved in the  
19 simulation of damage evolution with growth and remodeling; and (2) the nonlocal damage  
20 process is realized by introducing the gradient-enhanced variable, thus allowing the effect of  
21 internal length scales of soft tissues to be considered.

22 Uncertainty widely exists due to the variability in human tissues, such as the patient-  
23 dependent structural uncertainty and parametric uncertainty [14]. Parameter sensitivity  
24 analysis involving uncertainty is an essential step for developing and applying damage mod-  
25 els to soft biological tissues. For instance, parameter sensitivity is the key information  
26 for medical device approval [15]. Some probabilistic method-based models have been pre-  
27 sented to analyze the uncertainty of biomechanical problems. For instance, Laz and Browne  
28 [16] presented an overview of probability analysis in structural reliability, kinematics, joint  
29 mechanics, musculoskeletal modeling, and patient-specific representations. Regarding the  
30 uncertain damage analysis of soft tissues, Rodríguez et al. [17] presented a model taking  
31 into account a stochastically-distributed waviness and a subsequent rupture of the individual  
32 fibers as the main driving force for damage evolution, and Schmidt et al. [18] proposed a sta-  
33 tistical approach to describe the evolution of microscopic damage in soft collagenous tissues.  
34 More recently, [Balzani et al. \[19\]](#) introduced a computational method for the assessment of  
35 rupture probabilities in soft collagenous tissues based on the numerical minimization and  
36 maximization of the probability of failure (PoF), which arise from random input quanti-  
37 ties. Although the above models have been proposed to deal with the uncertainty analysis  
38 in biomechanics, there is still no work on the analysis of the uncertainty in the nonlocal  
39 damage model for soft biological tissues.

40 The large computational cost is a main challenge in uncertainty analysis when a prob-  
41 abilistic method is used [19, 20]. Although the Monte Carlo method is the most straight-  
42 forward way to conduct probability analysis [21], deterministic problems must usually be  
43 solved many times to guarantee the accuracy of the Monte Carlo method. Especially for the  
44 damage analysis for soft biological tissues, the computation of one deterministic problem  
45 usually requires considerable computational cost due to the solutions of nonlinear problems.  
46 Therefore, it is desirable to reduce the computational cost of uncertain damage analysis for  
47 soft biological tissues.

48 The surrogate model is an effective approach to reduce the computational cost of uncer-

49 tainty analysis [22]. The key idea of the surrogate model is to use an approximate model  
50 with rather a simple form to replace the original model by fitting the relationship between  
51 the input and output variables [23]. An overview of surrogate models can be found in the  
52 literatures provided by Díaz-Manríquez et al. [24], Razavi et al. [25], Asher et al. [26],  
53 Zhang [27] or Raul et al. [28]. The widely-used surrogate models include the following:  
54 polynomial approximation models [29], the radial basis function [30], Kriging models [31],  
55 etc. In this paper, the Legendre polynomial series surrogate model proposed by Wang et al.  
56 [32] is employed in the damage analysis of soft tissues due to its excellent error properties  
57 in the approximation of a globally smooth function [33].

58 To investigate the sensitivity of the uncertain material properties for the damage anal-  
59 ysis of soft tissues, a numerical analysis approach is developed by integrating the gradient-  
60 enhanced damage model [10, 11] and the Legendre polynomial series surrogate model [32]  
61 introduced above. The gradient-enhanced damage model is adopted to describe the behavior  
62 of the stress-softening of soft tissues and avoid mesh-dependence. The Legendre polynomial  
63 is used to replace the finite element method (FEM) solutions of deterministic problems, and  
64 the sparse grid collocation method (SGCM) is employed because of its advantage of using  
65 fewer collocation points when training surrogate models.

66 The remainder of this paper is organized as follows: Section 2 introduces the materials  
67 and methods, including the basic kinematics in Section 2.1, the gradient-enhanced damaged  
68 model in Section 2.2, the total potential energy and variational form in Section 2.3, the  
69 constitutive model in Section 2.4, the surrogate model in Section 2.5 and probability analysis  
70 in Section 2.6. Section 3 shows two numerical examples. Finally, discussions and conclusions  
71 are given in Section 4.

## 72 2. Methods and materials

### 73 2.1. Basic kinematics

74 Let  $\boldsymbol{x} = \boldsymbol{\varphi}(\boldsymbol{X}, t)$  describe the motion of a body from the initial reference configuration  
75  $\boldsymbol{X} \in \kappa(0)$  to its current configuration  $\boldsymbol{x} \in \kappa(t)$ . The deformation gradient  $\boldsymbol{F}$  and the  
76 Jacobian  $J$  that maps the referential volume  $dV$  onto the current volume  $dv$  are defined as

$$\boldsymbol{F} = \nabla_{\boldsymbol{X}} \boldsymbol{\varphi}, \quad (1)$$

$$J = \frac{dv}{dV} = \det(\boldsymbol{F}). \quad (2)$$

### 77 2.2. Gradient-enhanced damage model

78 The local strain energy function  $\Psi^{\text{loc}}$  per unit of reference volume at each time is written  
79 as

$$\Psi^{\text{loc}} = f(d)\Psi_0, \quad (3)$$

80 where  $\Psi_0$  is the original (undamaged) strain energy density and  $f(d)$  represents a function  
 81 of the damage variable  $d$  that measures the degree of material stiffness loss. In Eq. (3),  
 82  $f(d) = 1$  means there is no damage and the total damage for  $f(d) \rightarrow 0$ . It is at least twice  
 83 differentiable and satisfies the following conditions:

$$f(d) \quad : \quad \mathfrak{R}^+ \rightarrow (0, 1] \{f(0) = 1, \lim_{d \rightarrow \infty} f(d) = 0\}. \quad (4)$$

84 Following the approaches of Dimitrijevic and Hackl [10, 11], a gradient-enhanced nonlocal  
 85 free energy term is added to the strain energy given in Eq. (3)

$$\Psi = f(d)\Psi_0 + \frac{c_d}{2} \|\nabla_{\mathbf{x}}\phi\|^2 + \frac{\beta_d}{2} [\phi - \gamma_d d]^2. \quad (5)$$

86 In Eq. (5),  $c_d$  represents the gradient parameter that defines the degree of gradient  
 87 regularization and the internal length scales. Three other variables are introduced:

- 88 - the field variable  $\phi$ , which transfers the values of the damage parameter across the
- 89 element boundaries to make it non-local by nature;
- 90 - the energy-related penalty parameter  $\beta_d$ , which approximately forces the local damage
- 91 field and the nonlocal field to coincide; and
- 92 - parameter  $\gamma_d$ , which is set as a switch between the local and enhanced models. **When**
- 93  **$\gamma_d = 0$  and  $c_d = 0$ , it leads to a local model, while setting  $\gamma_d = 1$  and  $c_d \neq 0$  leads to the**
- 94 **enhanced non-local model. A typical value of this parameter is set to 1 following Dimitrijevic**
- 95 **and Hackl [10, 11] and Waffenschmidt et al. [34].**

### 96 2.3. Total potential energy and variational form

97 The general total potential energy for nonlocal damage model is

$$\Pi = \int_{\Omega} \Psi \, dV - \int_{\Omega} \bar{\mathbf{B}} \cdot \boldsymbol{\varphi} \, dV - \int_{\partial\Omega} \bar{\mathbf{T}} \cdot \boldsymbol{\varphi} \, dV, \quad (6)$$

98 where  $\bar{\mathbf{B}}$  is the body force vector per unit of reference volume of  $\Omega$  and  $\bar{\mathbf{T}}$  is the traction on  
 99 the boundary  $\partial\Omega$ .

100 Minimization of the potential energy with respect to the primal variables  $\boldsymbol{\varphi}$  and  $\phi$  results  
 101 in a coupled non-linear system of equations, which may be written as

$$\int_{\Omega} \mathbf{P} : \nabla_{\mathbf{x}} \delta \boldsymbol{\varphi} \, dV - \int_{\Omega} \bar{\mathbf{B}} \cdot \delta \boldsymbol{\varphi} \, dV - \int_{\partial\Omega} \bar{\mathbf{T}} \cdot \delta \boldsymbol{\varphi} \, dV = 0, \quad (7)$$

$$\int_{\Omega} \mathbf{Y} : \nabla_{\mathbf{x}} \delta \phi \, dV - \int_{\Omega} Y \delta \phi \, dV = 0, \quad (8)$$

102 where  $\mathbf{P}$  is the first Piola-Kirchhoff stress,  $\mathbf{Y}$  is vectorial damage quantity related to *flux*  
 103 terms and  $Y$  is the scalar damage quantity associated to *source* terms. They are defined as

$$\mathbf{P} = \partial_{\mathbf{F}} \Psi, \quad \mathbf{Y} = \partial_{\nabla_{\mathbf{x}} \phi} \Psi, \quad Y = -\partial_{\phi} \Psi. \quad (9)$$

104 The corresponding spatial quantities in Eq. (9) and the body force vector  $\bar{\mathbf{B}}$  are given  
 105 by

$$\boldsymbol{\sigma} = \mathbf{P} \cdot \text{cof}(\mathbf{F}^{-1}), \quad \bar{\mathbf{b}} = J^{-1}\bar{\mathbf{B}}, \quad (10)$$

$$\mathbf{y} = \mathbf{Y} \cdot \text{cof}(\mathbf{F}^{-1}), \quad y = J^{-1}Y, \quad (11)$$

106 where  $\text{cof}(\mathbf{F}) = J\mathbf{F}^{-\text{T}}$ .

107 Substituting Eqs. (2), (10) and (11) into Eqs. (7) and (8), the variational forms of the  
 108 spatial description are

$$\int_{\Omega} \boldsymbol{\sigma} : \nabla_{\mathbf{x}} \delta \boldsymbol{\varphi} \, dv - \int_{\Omega} \bar{\mathbf{b}} \cdot \delta \boldsymbol{\varphi} \, dv - \int_{\partial\Omega} \bar{\mathbf{t}} \cdot \delta \boldsymbol{\varphi} \, dv = 0, \quad (12)$$

$$\int_{\Omega} \mathbf{y} : \nabla_{\mathbf{x}} \delta \phi \, dv - \int_{\Omega} y \delta \phi \, dv = 0. \quad (13)$$

## 109 2.4. Constitutive model

### 110 2.4.1. Hyperelastic part of the free energy

111 For the undamaged part  $\Psi_0$  in Eq. (3), we used the Holzapfel-Gasser-Ogden (HGO)  
 112 hyperelastic constitutive model [35, 36], which can be written as

$$\Psi_0 = \Psi^{\text{iso}} + \Psi^{\text{aniso}}, \quad (14)$$

113 where the isotropic part  $\Psi^{\text{iso}}$  and anisotropic part  $\Psi^{\text{aniso}}$  are

$$\Psi^{\text{iso}} = \frac{1}{2}\mu_0 J^{-2/3}(I_1 - 3) + \frac{1}{2}\kappa_0(J - 1)^2, \quad (15)$$

$$\Psi^{\text{aniso}} = \frac{k_1}{2k_2} \sum_{i=4,6} [\exp(k_2 \langle E_i \rangle^2) - 1], \quad (16)$$

114 where  $\mu_0$  and  $\kappa_0$  are the shear and bulk moduli of the soft isotropic matrix, respectively.  
 115  $I_1 = \text{tr}(\mathbf{C})$  is the first invariant of  $\mathbf{C}$ , where  $\mathbf{C}$  is the right Cauchy-Green tensor, which is  
 116 defined as  $\mathbf{C} = \mathbf{F}^{\text{T}}\mathbf{F}$ . In Eq. (16),  $E_i = \varkappa I_1 + (1 - 3\varkappa)I_{4i} - 1$  is a strain-like quantity and  
 117 the  $I_{4i} = \mathbf{C} : \mathbf{A}_i = \mathbf{C} : (\mathbf{a}_{0i} \otimes \mathbf{a}_{0i})$  is the fourth invariant (which equals the square of the  
 118 stretch of collagen fibers), the  $\varkappa \in [0, 1/3]$  is a dispersion parameter and  $\mathbf{a}_{0i} = (\cos\theta, \sin\theta, 0)$   
 119 is the unit direction vector of the fiber in the reference configuration.  $k_1$  and  $k_2$  are material  
 120 parameters. The term  $\langle E_i \rangle$ , where  $\langle E_i \rangle = (|E_i| + E_i)/2$  is the Macaulay bracket,  
 121 reflects the basic assumption that fibers can only support tension.

122 *2.4.2. Damage evolution*

123 The detailed evolution of the damage variable  $d$  can be found in the works of Dimitrijevic  
 124 and Hackl [10, 11] and Waffenschmidt et al. [34]. In the following, we give a brief description  
 125 of some basic and essential formulations.

126 Following standard thermodynamic considerations [10, 11], the damage conjugate driving  
 127 force  $q$  is defined as

$$q = -\frac{\partial\Psi}{\partial d}. \quad (17)$$

128 The damage condition at any time of the loading process is based on an energy release  
 129 rate threshold condition [37]

$$\Phi_d = q - r_1 \leq 0, \quad (18)$$

130 where  $r_1$  represents the threshold value that triggers the evolution of the damage.

131 The differential equation of the evolution of damage is subjected to the Kuhn-Tucker  
 132 optimality conditions [10, 11]

$$\dot{d} = \dot{\kappa} \frac{\partial\Phi_d}{\partial q}, \quad \dot{\kappa} \geq 0, \quad \Phi_d \leq 0, \quad \dot{\kappa}\Phi_d = 0, \quad (19)$$

133 where  $\dot{\kappa}$  is the Lagrange multiplier.

134 *2.4.3. Verification of the damage model*

135 An exemplary qualitative simulation is applied here to show how this non-local damage  
 136 model can capture the stiffness loss of soft tissues when subjected to an overloading beyond  
 137 physiological loads, and the results are shown in Fig. 1. In this simulation, an exponential  
 138 damage function  $f(d) = e^{-d}$  was adopted and was also used in following simulations. Other  
 139 damage functions satisfying Eq. (4) could also be used [34]. The chosen model was compared  
 140 with experimental stress-strain responses of Raghavan et al. [38]. In these experimental data,  
 141 thin strips of abdominal aortic aneurysm excised from the anterior surface during surgical  
 142 repair were tested. Both the elastic and damage phases were well described by the non-local  
 143 damage model as shown in Fig. 1.

144 *2.5. Surrogate model*

145 *2.5.1. Legendre polynomial surrogate model*

146 In this paper, the Legendre polynomial surrogate model is used to approximate the  
 147 results of the FEM [32], and the Rodrigues formula of the  $N$ -order Legendre polynomial  
 148  $\Phi(\alpha)$  can be written as

$$\Phi(\alpha) = \frac{1}{2^N N!} \frac{d^N}{d(\alpha)} [((\alpha)^2 - 1)^N], \quad (20)$$

149 where  $\alpha$  is the uncertain variable and  $N$  is the order of the polynomial series.

150 Based on the polynomial chaos framework [39], the output variable  $L(\mathbf{x}, \boldsymbol{\alpha})$  can be  
 151 expressed as

$$L(\mathbf{x}, \boldsymbol{\alpha}) = \sum_{\mathbf{i}} w_{\mathbf{i}}(\mathbf{x}) \Phi_{\mathbf{i}}(\boldsymbol{\alpha}), \quad (21)$$

152 where  $\mathbf{x}$  is the spatial coordinate,  $\boldsymbol{\alpha}$  is the uncertain variables vector,  $w_{\mathbf{i}}(\mathbf{x})$  is the corre-  
 153 sponding expansion coefficient and  $\mathbf{i} = (i_1, i_2, \dots, i_n)$  stands for the multigauge. Note that  
 154  $L$  is the output variable, and it can be any variables concerned (stress and damage in this  
 155 paper). In practice, a maximum order of polynomials  $N$  is selected to truncate Eq. (21) up  
 156 to finite terms, by which Eq. (21) can be concisely rewritten as

$$L(\mathbf{x}, \boldsymbol{\alpha}) \approx L_N(\mathbf{x}, \boldsymbol{\alpha}) = \sum_{\mathbf{i} \leq N} w_{\mathbf{i}}(\mathbf{x}) \Phi_{\mathbf{i}}(\boldsymbol{\alpha}). \quad (22)$$

### 157 2.5.2. Sparse grid collocation method (SGCM)

158 The basic idea of a collocation method is using the response values at preselected points  
 159 in uncertainty space to calculate the expansion coefficients of the surrogate model [32]. In  
 160 this paper, the SGCM based on the Clenshaw-Curtis point-based collocation method and  
 161 the Smolyak algorithm is adopted with the advantage that it can minimize the collocation  
 162 error with the same number of nodes under the maximum norm [32].

163 For the univariate case, the Clenshaw-Curtis nodes distributed in the interval range  
 164  $[\underline{\alpha}_i, \bar{\alpha}_i]$  are defined as

$$\beta_j^i = \begin{cases} \alpha_i^c & \text{if } m_i = 1 \\ \alpha_i^c - \cos \frac{\pi(j-1)}{m_i-1} \cdot \Delta\alpha_i & \text{if } m_i > 1 \end{cases}, \quad (23)$$

165 where  $\alpha_i^c = (\bar{\alpha}_i + \underline{\alpha}_i)/2$ ,  $\Delta\alpha_i = (\bar{\alpha}_i - \underline{\alpha}_i)/2$ , in which  $\bar{\alpha}$  and  $\underline{\alpha}$  represents the upper bound  
 166 and lower bound of the uncertain interval, respectively,  $m_i$  is the predefined number of  
 167 collocation points.

168 For the multivariate case, the  $n$  input parameters are assumed to be independent with  
 169 each other for simplification. The general approach is to extend the collocation points defined  
 170 in one dimension in Eq. (23) to the entire interval uncertain space using a tensor product.  
 171 For each dimension, a nodal set  $\Theta_i^{m_i} = \{\beta_1^i, \beta_2^i, \dots, \beta_{m_i}^i\}$  is selected. On this basis, the entire  
 172 nodal set named the full tensor product grids can be denoted as

$$\Theta = \Theta_1^{m_1} \times \Theta_2^{m_2} \times \dots \times \Theta_n^{m_n}, \quad (24)$$

173 where the total number of collocation points  $M$  is

$$M = \prod_{i=1}^n m_i = m_1 \times m_2 \times \dots \times m_n. \quad (25)$$

174 To reduce the huge computational cost for high-dimensional problems, Smolyak-type  
 175 sparse grids [40] are introduced, which are still based on the tensor product construction,



176 but only a small subset of the full tensor grids Eq. (24) are selected. By using the Smolyak  
 177 algorithm, the total nodal set of collocation points in Eq. (24) can be reconstructed in the  
 178 following form:

$$\Theta = \bigcup_{l-n+1 \leq |\mathbf{i}| \leq l} (\Theta_1^{i_1} \times \Theta_2^{i_2} \times \dots \times \Theta_n^{i_n}), \quad (26)$$

179 where  $l \geq n$  is an integer representing the overall level of the construction and  $i_j$  represents  
 180 the separate level along the  $j$  th direction.

181 By iterating through all the nodes on full grids, only the ones whose sum order  $|\mathbf{i}| =$   
 182  $i_1 + i_2 + \dots + i_n$  across all dimensions is from  $l - n + 1$  to  $l$  are retained. To define the  
 183 collocation points, an index  $k$  is introduced to denote the level of collocation points in one-  
 184 dimensional uncertainty space. The number  $m_i^k$  and positions  $\beta_j^i$  of the Clenshaw-Curtis  
 185 nodes in the interval range  $[\underline{\alpha}_i, \overline{\alpha}_i]$  are defined as

$$m_i^k = \begin{cases} 1 & \text{if } k = 1 \\ 2^{k-1} + 1 & \text{if } k > 1 \end{cases} \quad (27)$$

$$\beta_j^i = \begin{cases} \alpha_i^c & \text{if } k = 1 \\ \alpha_i^c - \cos \frac{\pi(j-1)}{m_i^k-1} \cdot \Delta\alpha_i & \text{if } k > 1 \end{cases} \quad j = 1, 2, \dots, m_i^k$$

186 After selecting the SGCM nodal set, a set  $\Theta = \{\beta_1, \beta_2, \dots, \beta_M\}$  is given to specifically  
 187 denote all the collocation points in the interval uncertain space, and  $L(\mathbf{x}, \beta_j)$  is the solution  
 188 of the objective variable in the deterministic problem at the preselected points  $\beta_j$  that could  
 189 be obtained by the FEM. Based on the surrogate function in Eq. (22), a group of linear  
 190 equations with respect to the unknown expansion coefficients  $w_i(\mathbf{x})$  can be derived as

$$\begin{pmatrix} \Phi_1(\beta_1) & \Phi_2(\beta_1) & \dots & \Phi_{C_{n+N}^n}(\beta_1) \\ \Phi_1(\beta_2) & \Phi_2(\beta_2) & \dots & \Phi_{C_{n+N}^n}(\beta_2) \\ \vdots & \vdots & \ddots & \vdots \\ \Phi_1(\beta_M) & \Phi_2(\beta_M) & \dots & \Phi_{C_{n+N}^n}(\beta_M) \end{pmatrix} \begin{pmatrix} w_1(\mathbf{x}) \\ w_2(\mathbf{x}) \\ \vdots \\ w_{C_{n+N}^n}(\mathbf{x}) \end{pmatrix} = \begin{pmatrix} L(\mathbf{x}, \beta_1) \\ L(\mathbf{x}, \beta_2) \\ \vdots \\ L(\mathbf{x}, \beta_M) \end{pmatrix}. \quad (28)$$

191 Once the polynomial bases  $\Phi_i$  and the SGCM nodal set  $\Theta$  are given, the expansion  
 192 coefficients  $w_i(\mathbf{x})$  in Eq. (22) can be solved by Eq. (28). Note that the number of collocation  
 193 points is required not to be smaller than the number of polynomial expansion terms, such  
 194 as  $M \geq C_{n+N}^n$ , to prevent the problem from being undetermined.

## 195 2.6. Probability analysis

196 The prediction of the rupture of soft tissues with uncertain parameters can be captured  
 197 by the rupture probability, and PoF is defined as the probability that a mechanical rupture  
 198 criterion holds. Such a criterion can be formulated as the inequality  $f > f^{max}$ , where  $f$   
 199 represents a mechanical quantity of interest, for example, the stress, strain, or damage,  
 200 which is considered relevant for initializing a rupture [19].

201 Let  $\mathbf{R}$  be a set of input parameters and  $z(\mathbf{R})$  is the mechanical quantity of interest. A  
 202 suitable failure criterion can be defined as

$$z(\mathbf{R}) \geq z^{max}, \quad (29)$$

203 where  $z^{max}$  is a maximally admissible value. Generally, the PoF can be defined as

$$\text{PoF} := \mathbb{P}[z(\mathbf{R}) \geq z^{max}], \quad (30)$$

204 where  $\mathbb{P}(\cdot)$  is the probability of  $(\cdot)$ .

205 In this paper, the beta distribution is used for uncertain parameters to avoid some  
 206 possible unreasonable values of the distribution, that could be produced in a Gaussian  
 207 distribution [18]. The probability density function (PDF) of the beta distribution is defined  
 208 as [41]:

$$\text{PDF}(\alpha; a, b) = \frac{1}{B(a, b)} \alpha^{a-1} (1 - \alpha)^{b-1}, \quad (31)$$

209 where  $\alpha$  is the uncertain parameter,  $a$  and  $b$  denote two shape parameters and  $B(\cdot)$  is the  
 210 beta function. Note that some alternative distributions, e.g. the lognormal distribution [42],  
 211 could also be used for uncertain parameters.

212 In this paper, the damage function  $f(d)$  is used to describe the risk of the rupture, and  
 213 a lower value of  $f(d)$  means a higher risk of rupture. Here, the PoF is redefined as

$$\text{PoF} := \mathbb{P}[f(d) \leq f(d)^{max}]. \quad (32)$$

214 The PoF can be calculated as the integral of the PDF of the damage function  $f(d)$  from  
 215  $f(d) = 0$  up to  $f(d) = f(d)^{max}$  as

$$\text{PoF} := \mathbb{P}[f(d) \leq f(d)^{max}] = \int_0^{f(d)^{max}} \text{PDF}(f(d)) df(d). \quad (33)$$

216 An example is shown for the computation of the PoF in Fig. 2. The damage function  
 217 is assumed to obey a beta distribution as  $f(d) \sim B(4, 4)$  within the interval  $(0, 1]$  and the  
 218 maximum damage is set to  $f(d)^{max} = 0.5$ . With these assumptions, the value of the PoF  
 219 can be calculated as 0.5 according Eq. (33), which is equaling to the area of gray part in  
 220 Fig. 2.

### 221 3. Numerical examples

222 The gradient-enhanced damage model is implemented within the commercial finite ele-  
 223 ment software Abaqus/Standard by means of a user subroutine UEL and the simulation of  
 224 the probability analyses based on the surrogate model are carried out by Matlab R2018a.  
 225 Both computations are conducted on a PC with an Intel Xeon E5-2650 CPU @ 2.40 GHz  
 226 and 32 GB of RAM.

227 The first example is used to illustrate the nonlocal damage model and the advantages of  
 228 the surrogate model with the SGCM through an open-hole plate case. The second example  
 229 is a radial dilatation of an idealized artery, which is used to treat atherosclerotic plaque.  
 230 Note that only homogeneous uncertain material parameters without spatial correlation are  
 231 assumed for simplification, and plane strain elements (Bilinear 8 node element CPE8 in  
 232 Abaqus) are used in all simulations.

### 233 3.1. Open-hole plate

234 The first numerical example is an open-hole plate under displacement loading. The ge-  
 235 ometry and the FEM model are shown in Fig. 3. Due to the symmetry, only one-fourth of  
 236 the plate is analyzed. In this example, only the isotropic contribution of the soft tissues is  
 237 considered. The result of the deterministic analysis are shown in Section 3.1.1, the verifi-  
 238 cation of the surrogate model is shown in Section 3.1.2 and the results of the probability  
 239 analysis are shown in Section 3.1.3.

#### 240 3.1.1. Deterministic analysis

241 In this part, a series tests on 286 elements are performed, which the mesh-dependence  
 242 had been already examined in our previous works [12, 13], to investigate the influence of  
 243 the shear modulus and the internal length scales on the damage analysis in deterministic  
 244 problem. The geometry, hyperelastic and damage parameters are reported in Table 1, in  
 245 which the bulk modulus  $k_0$  is set to 100 times of the shear modulus to make the material  
 246 nearly incompressible.

247 The contours of the damage function  $f(d)$  for different shear modulus are shown in Fig. 4,  
 248 while the internal length scales is  $c_d = 1.0 \text{ MPa}^{-1} \cdot \text{mm}^2$ . It can be obviously seen that a  
 249 larger value of the shear modulus resulting a larger damage, and the same results can be  
 250 also observed in Fig. 5. The value of the parameter  $c_d$  represents the degree of regularization  
 251 and it depends on the microstructure of the tissues. The influence of the internal length  
 252 scales  $c_d$  is investigated by three different values and the results are shown in Figs. 6 and 7,  
 253 while the shear modulus is a constant that  $\mu_e = 0.1 \text{ MPa}$ . As shown in Figs. 6 and 7, the  
 254 levels of damage are strongly depending on the value of  $c_d$ . It can be explained by the width  
 255 of the activated zone [10, 11, 34]. With a smaller  $c_d$ , a smaller region is influenced by the  
 256 damage variable, resulting in more concentrated distribution of the damage.

#### 257 3.1.2. Verification of the surrogate model

258 In the training of the surrogate model, the 5-order Legendre polynomial series and the  
 259 SGCM with  $k = 4$  are used. The comparison of the values of  $f(d)$  and  $\sigma_x$  computed by the  
 260 surrogate model and the FEM at six feature nodes (the locations are shown in Fig. 3(b))  
 261 for Case 1 when the stretch is  $\lambda_x = 0.1$  are listed in Table 3. A good agreement can be  
 262 seen in Table 3 such that the surrogate model with the SGCM can approximate the results  
 263 of the FEM with the maximum difference being less than 1%. The good performance of  
 264 the surrogate model with the SGCM is addressed again by comparing the results of the  
 265 surrogate model with the SGCM and FEM at Node 1 when  $\lambda_x = 0.1$  for Case 2 and Case  
 266 3, and the results are shown in Fig. 8.

267 *3.1.3. Probability analysis*

268 In this example, shear modulus  $\mu_e$  and internal length scales  $c_d$  are assumed to be  
 269 uncertain parameters that obey the beta distributions in the given intervals ( $\mu_e \in [0.07, 0.13]$   
 270 MPa and  $c_d \in [0.5, 1.5]$  MPa $^{-1} \cdot$  mm $^2$ ), and seven cases for different levels of uncertainty for  
 271  $\mu_e$  and  $c_d$  listed in Table 2 are analyzed. The bulk modulus  $k_0$  is set to 100 times of the  
 272 mean value of the shear modulus to make the material nearly incompressible. Apart from  
 273  $\mu_e$ ,  $c_d$  and  $k_0$ , other geometric and material parameters are shown in Table 1.

274 First, we investigate the computational cost for using the Monte Carlo method based  
 275 on the direct FEM and the Monte Carlo method based on the surrogate model. When  
 276 employing the Monte Carlo method,  $10^5$  samples are computed to ensure the accuracy of  
 277 the probability analysis, as suggested by Wu et al. [43]. The comparison of the CPU times  
 278 is shown in Table 4. Note that the computational time for the Monte Carlo method with  
 279 the direct FEM is estimated by multiplying the time of one FEM by  $10^5$ . A significant  
 280 reduction of the computational cost can be observed in Table 4 such that the computing  
 281 time of the Monte Carlo method with the surrogate model is about 0.06% of that using the  
 282 Monte Carlo method with the direct FEM but the relative error is less than 1%.

283 Second, the individual and combined impacts of the uncertain parameters on the evo-  
 284 lution of the damage are investigated through three different cases and the PDFs of the  
 285 damage function  $f(d)$  at Node 3 (the location is shown in Fig. 3(b)) are shown in Fig. 9(a).  
 286 Comparing Case 1 and 2, the mean value  $\hat{\mu}$  of the damage function  $f(d)$  is close but the  
 287 standard deviation  $\hat{\sigma}$  for Case 1 is larger than that for Case 2, which means that the shear  
 288 modulus  $\mu_e$  has a relatively larger influence on  $f(d)$  than the internal length scales  $c_d$  in this  
 289 example. For Case 3, a larger standard deviation  $\hat{\sigma} = 0.087$  can be found as expected and  
 290 there is little difference in the mean value  $\hat{\mu}$  between Case 1 and 2.

291 Third, the comparisons of the probabilistic damage analysis under uncertain parameters  
 292 on different points are provided by selecting three feature nodes (the locations are shown  
 293 in Fig. 3(b)), and only Case 3 is investigated with the results shown in Fig. 9(b). From  
 294 Fig. 9(b), Node 1 is the location where the damage is largest and the distribution of  $f(d)$   
 295 varies in a smaller range (the standard deviation is  $\hat{\sigma} = 0.030$ ). Comparing Nodes 1, 2  
 296 and 3, it can be found that the location with less damage is more sensitive to the uncertain  
 297 parameters, and the sensitivity increases as the damage level increases such that the standard  
 298 deviation  $\hat{\sigma}$  of the damage function  $f(d)$  increases from 0.03 to 0.087 when the mean value  
 299  $\hat{\mu}$  of  $f(d)$  increases from 0.066 to 0.41.

300 Finally, the levels of uncertainty for parameters are also investigated and the results are  
 301 shown in Figs. 9(c) and 9(d). Cases 4-6 are tested to illustrate the influence of the standard  
 302 deviation  $\hat{\sigma}$  when the mean value  $\hat{\mu}$  is the same. It can be seen in Fig. 9(c) that when the  
 303 mean value of the uncertain parameters is constant, the mean value of the damage function  
 304  $f(d)$  changes slightly, and the standard deviation of  $f(d)$  increases as the standard deviation  
 305 of the uncertain input parameters increases. The influence of the mean value of the input  
 306 parameters is also investigated in Fig. 9(d). It can be seen that the change of the mean  
 307 value of the input parameters may affect the distribution of the damage function  $f(d)$  such  
 308 that a larger mean value of the input parameters leads to more serious damage and the  
 309 distribution of the damage function will be more concentrated.

### 310 3.2. Radial dilatation of an idealized artery

311 The second example is damage analysis for radial dilatation of an idealized artery. The  
312 two-dimensional geometry and FEM mesh shown in Fig. 10 were previously established by  
313 Badel et al. [44] according to histological pictures of epicardial coronary arteries from Viles-  
314 Gonzalez et al. [45]. The artery is assumed to consist of a single medial layer containing  
315 an atherosclerotic plaque, and the balloon used for the angioplasty is modeled as a thin  
316 circular structure whose diameter increases during the angioplasty process. In this example,  
317 the damage is assumed to only occur in the artery. Based on the experiment data for human  
318 thoracic and abdominal aortas in Weisbecker et al. [46], the shear modulus of the artery is  
319 assumed obeys a beta distribution  $\mu_e \sim B(2.98, 8.72)$  within the interval [15,55] kPa. The  
320 internal length scales  $c_d$  is assumed to obey a beta distribution  $c_d \sim B(4, 4)$  within the  
321 interval [0.005, 0.015]  $\text{kPa}^{-1} \cdot \text{mm}^2$ .

322 In this simulation, some simplifications are assumed, i.e., the influence of the residual  
323 stresses, smooth muscle, lipid pool, and the image-based layer-specific structure of the ar-  
324 teries are not considered, and an idealized geometric shape is used. The only boundary  
325 conditions to be assigned are the nodal displacements of the balloon. A radial displacement  
326 is imposed on each node from its initial position,  $D_i = 1$  mm, to give a final deformed  
327 diameter,  $D_f = 2$  mm, where the center of the balloon is fixed. In the following, we use an  
328 inflation progress parameter  $\lambda = (D - D_i)/(D_f - D_i) \times 100\%$ , where  $D$  is the current diam-  
329 eter of the balloon, to denote the inflation progress. Note that all the degrees of freedom of  
330 the balloon are prescribed as displacement boundary conditions, and the artery is inflated  
331 by the contact between the balloon and artery. The contact problems (balloon and plaque,  
332 balloon and artery, plaque and artery) are assumed to be frictionless following Badel et al.  
333 [44] and are modeled as ‘Hard contact’ in Abaqus. The material parameters used in this  
334 example shown in Table 5 are according to Badel et al. [44] and Weisbecker et al. [46].

#### 335 3.2.1. Verification of the surrogate model

336 Similar with the previous example, three different cases, including (1)  $\mu_e$  is uncertain with  
337 a constant  $c_d$ , (2)  $c_d$  is uncertain with a constant  $\mu_e$  and (3) both  $\mu_e$  and  $c_d$  are uncertain,  
338 are tested and the distributions of the uncertain input parameters are shown in Table 6. The  
339 5-order Legendre polynomial surrogate model is used and the SGCM is set by setting  $k = 5$ .  
340 To check the accuracy of surrogate model, the damage function  $f(d)$  is calculated by the  
341 surrogate model and the direct FEM for 3 cases, and the results shown in Fig. 11 illustrate  
342 the good performance of the surrogate model. The contours of the damage function  $f(d)$   
343 calculated by the surrogate model with SGCM and FEM for different shear modulus and  
344 the internal length scales when  $\lambda = 100\%$  in Fig. 12 demonstrate the good performance of  
345 the surrogate model once again.

#### 346 3.2.2. Probability analysis

347 First, the computational cost of probability analysis for using the Monte Carlo method  
348 with the direct FEM and the Monte Carlo method with the surrogate model are investigated  
349 in Table 7. The results again demonstrate that the surrogate model can effectively reduce  
350 the computational cost with good accuracy, as shown in Fig. 11.

351 Second, the individual and combined impacts of the uncertain parameters on the damage  
352 are tested, and the PDFs of the damage function  $f(d)$  for three cases in Table 6 at different  
353 nodes (the locations are shown in Fig. 10) are shown in Fig. 13. Note that Node 1 is the  
354 location where the damage is the largest in the whole domain and it is selected through a  
355 previous simulation. For these three cases, the distribution of the damage function at Node  
356 1 is closer to 0, which means larger damage. Comparing the results of Case 1 for these three  
357 nodes, the same results that a larger influence of the shear modulus on the location with  
358 less damage can be observed, which the standard deviation  $\hat{\sigma}$  of the damage function  $f(d)$   
359 increase form 0.009 to 0.054. By comparing the results of  $f(d)$  for Cases 1 and 3 for these  
360 three nodes, only a visible difference at Node 1 can be found and  $f(d)$  varies in a larger  
361 range at Node 1 for Case 2 ( $\hat{\sigma} = 0.019$ ), which illustrates that value of the internal length  
362 scales  $c_d$  has a larger impact on the location with larger damage.

363 Moreover, three different ranges of the internal length scales  $c_d$ , that  $c_d \in [0.002, 0.018]$ ,  
364  $c_d \in [0.005, 0.015]$  and  $c_d \in [0.008, 0.012]$ , are tested to investigate the influence of the  
365 nonlocal damage parameter when  $\lambda = 100\%$ . In this situation, the shear modulus of the  
366 artery remains a constant such that  $\mu_e = 28.97$  kPa, and the PDF of  $f(d)$  at Node 1 is  
367 shown in Fig. 14(a). The value of the damage function  $f(d)$  varies in the range of  $f(d) \in$   
368  $[0.20, 0.25]$  when  $c_d \in [0.008, 0.012]$ , and the interval of the damage for  $c_d \in [0.002, 0.018]$  is  
369  $f(d) \in [0.10, 0.31]$ , which is 3 times larger than the width when  $c_d \in [0.008, 0.012]$ . Although  
370 the mean values of the PDFs of the damage function  $f(d)$  are close, the standard derivation  
371 increases from 0.011 to 0.029. When the range of  $c_d$  is larger, the damage function will  
372 be distributed over a larger interval. To evaluate the risk of an artery rupture, the PoF is  
373 calculated as introduced in Section 2.6. In this example, the maximum damage threshold  
374 is set to  $f(d)^{max} = 0.5$  in Eq. (32), which means that an artery rupture could occur when  
375  $f(d) \leq f(d)^{max}$ . Since Node 2 is the location where the damage is the largest, the PoF  
376 of the artery for Case 3 is calculated by integrating the PDF of the damage function  $f(d)$  at  
377 Node 2 from  $f(d) = 0$  to  $f(d) = 0.5$  through Eq. (33). When  $f(d)^{max} = 0.5$  and  $\lambda = 100\%$ ,  
378 the PoF of the artery is 1.0, which means that when  $\lambda = 100\%$ , there is a 100% chance of a  
379 rupture during the treatment.

380 As the size of the inflation of the balloon is the critical indicator in clinical treatment [47],  
381 the propagation of the uncertainty of the damage function  $f(d)$  with uncertain parameters  
382 under different inflation sizes is calculated. Four different inflation progress parameters  $\lambda$   
383 are used to study the influence of  $\lambda$  on the PoF of the artery, and the results are shown in  
384 Fig. 14(b). It can be seen that the PoF of  $f(d)$  is directly influenced by the inflation progress  
385 parameter  $\lambda$ . For instance, the PoF are 0.03 and 0.91 for  $\lambda = 90\%$  and  $\lambda = 95\%$ , respectively.  
386 Obviously, the PoF of the artery increases as the balloon inflation size increases.

#### 387 4. Discussion and conclusions

388 Due to the widely-existing uncertainty in damage analysis for soft biological tissues,  
389 the sensitivity analysis of nonlocal damage for soft biological tissues is an essential step  
390 in model development and application. To investigate the influence of the uncertain input  
391 parameters on the mechanical environment of the soft biological tissues, a numerical analysis

392 is conducted by combining the gradient-enhanced damage model [10, 11] and the surrogate  
393 model-based probability analysis method [33].

394 The first advantage of the presented model is that it can assess nonlocal damage with  
395 uncertain material parameters, including internal length scales. In our previous works [12,  
396 13], it was proved that the internal length scales have obvious effects on the localization  
397 of damage, e.g., a larger internal length scales lead to a larger lower level of damage and  
398 activated zone. In this paper, the influence of uncertain internal length scales can be analyzed  
399 by the proposed model. Therefore, it is possible to provide probabilistic results of the levels  
400 of damage, stress and deformation for soft tissue if the internal length scales are uncertain  
401 variables obeying a probability distribution. Moreover, the proposed model can consider the  
402 combined effects of different uncertain material parameters. For instance, both the shear  
403 modulus and an internal length scales parameter can be set as uncertain variables at the  
404 same time. This will be useful for dealing with the cases in which more uncertain parameters  
405 exist together.

406 The other advantage is that this paper's method provides a new approach for the un-  
407 certain damage analysis of soft biological tissues based on the surrogate model. Although  
408 the Monte Carlo method is an accurate and robust method for uncertainty analysis, the  
409 huge computational cost is a key challenge for its application to damage analyses since the  
410 nonlinear problem has to be repeatedly solved by the FEM [48, 49]. Due to the huge com-  
411 putational cost, the Monte Carlo method is commonly introduced as a referenced approach,  
412 but it is rarely used in the practical engineering. In this paper, the surrogate model based on  
413 the Legendre polynomial series was adopted to approximate the results of the FEM. When  
414 training of the surrogate model, the SGCM is employed to accelerate the procedure. First, it  
415 is demonstrated that the surrogate model has good accuracy compared with direct FEM so-  
416 lutions. For example, the maximum error is less than 1% compared with the results (Cauchy  
417 stress and the damage function) obtained from the surrogate model and the FEM at some  
418 feature nodes in the open-hole plate. Second, the surrogate model significantly improved  
419 the computational efficiency of the Monte Carlo method. For example, in the open-hole  
420 plate problem, the computational cost for the Monte Carlo method with the direct FEM  
421 was about 40 days, but the time for the surrogate model with the SGCM including training  
422 the surrogate model and probability analysis was only 0.63 h with a 286 elements mesh.

423 The proposed approach was applied to the simulation of the radial dilatation of an ideal-  
424 ized artery by considering the uncertain shear modulus and internal length scales. Although  
425 some simplifications are assumed, some interesting results are found: (1) the spatial posi-  
426 tions and level of damage could have significant impact on the uncertainty propagation of  
427 damage, for instance, the mean value and standard deviation are obviously different at dif-  
428 ferent locations (Node 1, Node 2 and Node 3) in Fig. 13; (2) different parameters could also  
429 have obviously different impact on the uncertainty propagation of damage. For instance, if  
430 only the uncertain shear modulus is considered (Case 1), a smaller standard deviation of  
431 damage is produced at Node 1 with larger damage compared with Node 3, while the internal  
432 length scales has an opposite trend with a larger standard deviation at Node 1 compared  
433 with Node 3 in Case 2; (3) although the PoF is increased with the increase of inflation size  
434 as expected, the relation between uncertain parameter and resulted PoF could still provide

435 a potential helpful approach for both directly predicting the PoF in clinical operation and  
436 inversely choosing the inflation size under a prescribed PoF.

437 The main limitation in this paper is that only 2D models and an idealized geometric  
438 model was considered. The development of a 3D patient-specific model is currently under  
439 progress in order to address more realistic applications. Meanwhile, some important aspects,  
440 such as the influence of the residual stresses, the smooth muscle activation, the lipid pool  
441 should also be considered. Besides, some uncertainty analyses about the geometry and  
442 the material parameters of the plaque, which is important in predicting the rupture risk  
443 of the artery, should be conducted, and the spatial uncertainty should also be considered  
444 as arteries are usually heterogeneous materials [50, 51]. Moreover, there is still a pressing  
445 need to develop further experiments to identify the distribution of shear moduli, the internal  
446 length scales and other unknown material parameters. Furthermore, the use of UEL presents  
447 some limitations such as, for instance, the definition of slave surfaces in contact analyses.

448 In summary, we have coupled a nonlocal damage model and a surrogate model to in-  
449 vestigate the influence of uncertainty on damage in soft tissues. The Legendre polynomial  
450 surrogate model with the SGCM was adopted in this paper to speed up the computation  
451 efficiency. The evolution of the PDF of the damage function  $f(d)$  was illustrated through  
452 two examples where the input parameters were assumed to be uncertain, and the method's  
453 clinical application to balloon angioplasty was also addressed. Future work will consist of  
454 applying the proposed model to practical problems by collecting clinical data.

## 455 Acknowledgments

456 The research leading to this paper was funded by the NSFC Grant [12072063], ERC-  
457 2014-CoG-BIOLOCHANICS [647067], grants from the State Key Laboratory of Structural  
458 Analysis for Industrial Equipment [S18402, GZ19105], the Liaoning Provincial Natural Sci-  
459 ence Foundation [2020-MS-110] and the Visiting Scholar Foundation of Key Laboratory of  
460 Biorheological Science and Technology (Chongqing University) from Ministry of Education  
461 [CQKLBST-2020-002].

## 462 References

- 463 [1] Mousavi SJ, Farzaneh S, Avril S. Computational predictions of damage propagation preceding dissection  
464 of ascending thoracic aortic aneurysms. *International journal for numerical methods in biomedical*  
465 *engineering* 2018; 34(4): e2944.
- 466 [2] Fleischmann W, Strecker W, Bombelli M, Kinzl L. Vacuum sealing as treatment of soft tissue damage  
467 in open fractures. *Der Unfallchirurg* 1993; 96(9): 488–492.
- 468 [3] Kloner R, Ellis S, Lange R, Braunwald E. Studies of experimental coronary artery reperfusion. Effects on  
469 infarct size, myocardial function, biochemistry, ultrastructure and microvascular damage.. *Circulation*  
470 1983; 68(2 Pt 2): I8–15.
- 471 [4] Holzapfel GA, Fereidoonzehad B. Modeling of damage in soft biological tissues. In: Elsevier. 2017  
472 (pp. 101–123).
- 473 [5] Trabelsi O, Davis FM, Rodriguez-Matas JF, Duprey A, Avril S. Patient specific stress and rupture  
474 analysis of ascending thoracic aneurysms. *Journal of biomechanics* 2015; 48(10): 1836–1843.
- 475 [6] Svensson R, Mulder H, Kovanen V, Magnusson SP. Fracture Mechanics of Collagen Fibrils: Influence  
476 of Natural Cross-Links. *Biophysical Journal* 2013; 104(11): 2476–2484.



- 477 [7] Holzapfel GA, Stadler M, Gasser TC. Changes in the mechanical environment of stenotic arteries during  
478 interaction with stents: computational assessment of parametric stent designs. *Journal of biomechanical*  
479 *engineering* 2005; 127(1): 166–180.
- 480 [8] Gasser TC. Damage in vascular tissues and its modeling. In: Springer. 2017 (pp. 85–118).
- 481 [9] Li , Wenguang . Damage Models for Soft Tissues: A Survey. *Journal of Medical & Biological Engineering*  
482 2016; 36(3): 285-307.
- 483 [10] Dimitrijevic B, Hackl K. A method for gradient enhancement of continuum damage models. *Technische*  
484 *Mechanik* 2008; 28(1): 43–52.
- 485 [11] Dimitrijevic B, Hackl K. A regularization framework for damage–plasticity models via gradient en-  
486 hancement of the free energy. *International Journal for Numerical Methods in Biomedical Engineering*  
487 2011; 27(8): 1199–1210.
- 488 [12] He Y, Zuo D, Hackl K, Yang H, Mousavi SJ, Avril S. Gradient-enhanced continuum models of healing  
489 in damaged soft tissues. *Biomechanics and Modeling in Mechanobiology* 2019; 18: 1–18.
- 490 [13] Zuo D, Avril S, Yang H, Mousavi SJ, Hackl K, He Y. Three-dimensional numerical simulation of  
491 soft-tissue wound healing using constrained-mixture anisotropic hyperelasticity and gradient-enhanced  
492 damage mechanics. *Journal of the Royal Society Interface* 2020; 17(162): 20190708.
- 493 [14] Paul H, Hale JS, Stéphane C, Bordas SPA. Quantifying the uncertainty in a hyperelastic soft tissue  
494 model with stochastic parameters. *Applied Mathematical Modelling* 2018; 62: 86-102.
- 495 [15] Gasser TC, Grytsan A. Biomechanical modeling the adaptation of soft biological tissue. *Current Opin-*  
496 *ion in Biomedical Engineering* 2017: S2468451117300272.
- 497 [16] Laz PJ, Browne M. A review of probabilistic analysis in orthopaedic biomechanics. *Proceedings of the*  
498 *Institution of Mechanical Engineers, Part H: Journal of Engineering in Medicine* 2010; 224(8): 927–943.
- 499 [17] Rodríguez JF, Cacho F, Bea JA, Doblaré M. A stochastic-structurally based three dimensional finite-  
500 strain damage model for fibrous soft tissue. *Journal of the Mechanics and Physics of Solids* 2006; 54(4):  
501 864–886.
- 502 [18] Schmidt T, Balzani D, Holzapfel GA. Statistical approach for a continuum description of damage  
503 evolution in soft collagenous tissues. *Computer Methods in Applied Mechanics and Engineering* 2014;  
504 278: 41–61.
- 505 [19] Balzani D, Schmidt T, Ortiz M. Method for the quantification of rupture probability in soft collagenous  
506 tissues. *International journal for numerical methods in biomedical engineering* 2017; 33(1): e02781.
- 507 [20] Lee T, Bilonis I, Tepole AB. Propagation of uncertainty in the mechanical and biological response  
508 of growing tissues using multi-fidelity Gaussian process regression. *Computer Methods in Applied Me-*  
509 *chanics and Engineering* 2020; 359: 112724.
- 510 [21] Fishman G. *Monte Carlo: concepts, algorithms, and applications*. Springer Science & Business Media  
511 . 2013.
- 512 [22] Ong YS, Nair PB, Keane AJ. Evolutionary optimization of computationally expensive problems via  
513 surrogate modeling. *AIAA journal* 2003; 41(4): 687–696.
- 514 [23] Gorissen D, Couckuyt I, Demeester P, Dhaene T, Crombecq K. A surrogate modeling and adaptive  
515 sampling toolbox for computer based design. *Journal of Machine Learning Research* 2010; 11(Jul):  
516 2051–2055.
- 517 [24] Díaz-Manríquez A, Toscano G, Barron-Zambrano JH, Tello-Leal E. A review of surrogate assisted  
518 multiobjective evolutionary algorithms. *Computational intelligence and neuroscience* 2016; 2016.
- 519 [25] Razavi S. Review of surrogate modeling in water resources. *Water Resources Research* 2012.
- 520 [26] Asher MJ, Croke BFW, Jakeman AJ, Peeters LJM. A review of surrogate models and their application  
521 to groundwater modeling. *Water Resources Research* 2015; 51(8): 5957-5973.
- 522 [27] Zhang W. *A Review of Surrogate Models*: 7–17; Singapore: Springer Singapore . 2020
- 523 [28] Yondo R, Bobrowski K, Andrés E, Valero E. *A Review of Surrogate Modeling Techniques for Aero-*  
524 *dynamic Analysis and Optimization: Current Limitations and Future Challenges in Industry*: 19–33;  
525 Cham: Springer International Publishing . 2019
- 526 [29] Myers RH, Montgomery DC, Anderson-Cook CM. *Response surface methodology: process and product*  
527 *optimization using designed experiments*. John Wiley & Sons . 2016.

- 528 [30] Hardy RL. Multiquadric equations of topography and other irregular surfaces. *Journal of geophysical*  
529 *research* 1971; 76(8): 1905–1915.
- 530 [31] Sacks J, Welch WJ, Mitchell TJ, Wynn HP. Design and analysis of computer experiments. *Statistical*  
531 *science* 1989: 409–423.
- 532 [32] Wang C, Qiu Z, Yang Y. Collocation methods for uncertain heat convection-diffusion problem with  
533 interval input parameters. *International Journal of Thermal Sciences* 2016; 107: 230–236.
- 534 [33] Wang H, Xiang S. On the convergence rates of Legendre approximation. *Mathematics of Computation*  
535 2012; 81(278): 861–877.
- 536 [34] Waffenschmidt T, Polindara C, Menzel A, Blanco S. A gradient-enhanced large-deformation continuum  
537 damage model for fibre-reinforced materials. *Computer Methods in Applied Mechanics and Engineering*  
538 2014; 268: 801–842.
- 539 [35] Holzapfel GA, Gasser TC, Ogden RW. A New Constitutive Framework for Arterial Wall Mechanics  
540 and a Comparative Study of Material Models. *Journal of Elasticity* 2000; 61(1-3): 1-48.
- 541 [36] Gasser TC, Ogden RW, Holzapfel GA. Hyperelastic modelling of arterial layers with distributed collagen  
542 fibre orientations. *Journal of the Royal Society Interface* 2006; 3(6).
- 543 [37] Simo JC, Ju J. Strain-and stress-based continuum damage models—I. Formulation. *International jour-*  
544 *nal of solids and structures* 1987; 23(7): 821–840.
- 545 [38] Raghavan ML, Webster MW, Vorp DA. Ex vivo biomechanical behavior of abdominal aortic aneurysm:  
546 assessment using a new mathematical model.. *Annals of Biomedical Engineering* 1996; 24(5): 573-582.
- 547 [39] Xiu D, Karniadakis GE. Modeling uncertainty in flow simulations via generalized polynomial chaos.  
548 *Journal of computational physics* 2003; 187(1): 137–167.
- 549 [40] Smolyak S. Quadrature and Interpolation Formulas for Tensor Products of Certain Classes of Functions.  
550 *Doklady Akademii Nauk Sssr* 1963; 4(5): 240-243.
- 551 [41] Johnson NL, Kotz S, Balakrishnan N. *Continuous univariate distributions*. Houghton Mifflin . 1970.
- 552 [42] Biehler J, Wall W. The impact of personalized probabilistic wall thickness models on peak wall stress  
553 in abdominal aortic aneurysms. *International journal for numerical methods in biomedical engineering*  
554 2018; 34(2): e2922.
- 555 [43] Wu D, Gao W, Wang C, Tangaramvong S, Tin-Loi F. Robust fuzzy structural safety assessment using  
556 mathematical programming approach. *Fuzzy Sets & Systems* 2016; 293(jun.15): 30-49.
- 557 [44] Badel P, Avril S, Sutton MA, Lessner SM. Numerical simulation of arterial dissection during balloon  
558 angioplasty of atherosclerotic coronary arteries. *Journal of biomechanics* 2014; 47(4): 878–889.
- 559 [45] Viles-Gonzalez JF, Castro Miranda dR, Scanavacca M, Sosa E, d’Avila A. Acute and chronic effects of  
560 epicardial radiofrequency applications delivered on epicardial coronary arteries. *Circulation: Arrhyth-*  
561 *mia and Electrophysiology* 2011; 4(4): 526–531.
- 562 [46] Weisbecker H, Pierce DM, Regitnig P, Holzapfel GA. Layer-specific damage experiments and modeling  
563 of human thoracic and abdominal aortas with non-atherosclerotic intimal thickening. *Journal of the*  
564 *mechanical behavior of biomedical materials* 2012; 12: 93–106.
- 565 [47] Tenaglia AN, others . Intravascular ultrasound and balloon percutaneous transluminal coronary angio-  
566 plasty. *Cardiology clinics* 1997; 15(1): 31–38.
- 567 [48] Neumaier A. *Interval methods for systems of equations*. 37. Cambridge university press . 1990.
- 568 [49] Ran C, Yang H, Zhang G. A gradient based algorithm to solve inverse plane bimodular problems of  
569 identification. *Journal of Computational Physics* 2018; 355: 78–94.
- 570 [50] Bersi MR, Bellini C, Di Achille P, Humphrey JD, Genovese K, Avril S. Novel Methodology for Char-  
571 acterizing Regional Variations in the Material Properties of Murine Aortas. *Journal of Biomechanical*  
572 *Engineering* 2016; 138(7). 071005.
- 573 [51] Bersi MR, Santamaría VAA, Marback K, Achille PD, Avril S. Multimodality Imaging-Based Charac-  
574 terization of Regional Material Properties in a Murine Model of Aortic Dissection. *Scientific Reports*  
575 2020; 10(1).

576 **List of Tables**

577	1	Geometry, hyperelastic and damage parameters used in the open-hole plate.	19
578	2	The uncertain input parameters for different cases. . . . .	20
579	3	Comparison of the results obtained by the FEM and surrogate model with the SGCM when $\lambda_x = 0.1$ for Case 1. . . . .	21
580			
581	4	The comparison of the computational cost between using the Monte Carlo method with the direct FEM and the Monte Carlo method with the surrogate model. . . . .	22
582			
583			
584	5	Hyperelastic and damage parameters used in the radial dilatation of an idealized artery [44, 46]. . . . .	23
585			
586	6	The uncertain input parameters for different cases. . . . .	24
587	7	The comparison of the computational cost between using the Monte Carlo method with the direct FEM and the Monte Carlo method with the surrogate model. . . . .	25
588			
589			

Table 1: Geometry, hyperelastic and damage parameters used in the open-hole plate.

Type	Description	Symbol	Values	Units
Geometric	Height	H	200	mm
	Width	W	200	mm
	Radius	R	50	mm
Hyperelastic	Shear modulus	$\mu_0$	[0.5,1.0,1.5]	MPa
	Bulk modulus	$\kappa_0$	[5,10,15]	MPa
Damage	Damage threshold	$r_1$	0.001	MPa
	Internal length scales	$c_d$	[0.5,1,5]	MPa <sup>-1</sup> · mm <sup>2</sup>
	Penalty parameter	$\beta_d$	0.005	MPa <sup>-1</sup>
	(Non)local switch	$\gamma_d$	1	-

Table 2: The uncertain input parameters for different cases.

Case	$\mu_e$ (MPa)			$c_d$ (MPa <sup>-1</sup> · mm <sup>2</sup> )		
	Distribution	Mean	Standard Deviation	Distribution	Mean	Standard Deviation
1	$B(4,4)$	0.1	0.01	-	1	-
2	-	0.1	-	$B(4,4)$	1	0.17
3	$B(4,4)$	0.1	0.01	$B(4,4)$	1	0.17
4	$B(2,2)$	0.1	0.013	$B(2,2)$	1	0.22
5	$B(8,8)$	0.1	0.0073	$B(8,8)$	1	0.12
6	$B(4,2)$	0.11	0.0107	$B(4,2)$	1.17	0.18
7	$B(2,4)$	0.09	0.0107	$B(2,4)$	0.83	0.18

Table 3: Comparison of the results obtained by the FEM and surrogate model with the SGCM when  $\lambda_x = 0.1$  for Case 1.

Node	$\mu_e$	FEM		SGCM			
		$f(d)$	$\sigma_x$	$f(d)$	error	$\sigma_x$	error
1	0.08	0.142469	0.028497	0.141972	0.35%	0.028479	0.06%
	0.12	0.028766	0.026306	0.028787	0.07%	0.026207	0.38%
2	0.08	0.38338	0.031512	0.382846	0.14%	0.031431	0.26%
	0.12	0.161063	0.031508	0.161157	0.06%	0.03152	0.04%
3	0.08	0.607423	0.014506	0.605692	0.28%	0.014729	0.05%
	0.12	0.293042	0.015549	0.294017	0.33%	0.015552	0.02%
4	0.08	1	0.001851	1	0.00%	0.001855	0.23%
	0.12	1	0.001331	1	0.00%	0.001342	0.80%
5	0.08	1	-0.00159	1	0.00%	-0.00159	0.10%
	0.12	1	-0.00086	1	0.00%	-0.00086	0.20%
6	0.08	1	0.022613	1	0.00%	0.022606	0.03%
	0.12	1	0.021469	1	0.00%	0.02149	0.10%

Table 4: The comparison of the computational cost between using the Monte Carlo method with the direct FEM and the Monte Carlo method with the surrogate model.

	Monte Carlo method with the direct FEM (Estimated, $t_1$ )	Monte Carlo method with the surrogate model			$t_2/t_1$
		Training the surrogate model	Probability analysis	Total time ( $t_2$ )	
79 elements	14.70 days	825 sec	11.82 sec	836.82 sec	0.06%
286 elements	40.05 days	2249 sec	36.28 sec	2285.28 sec	0.07%
793 elements	115.27 days	6474 sec	98.73 sec	6572.73 sec	0.07%

Table 5: Hyperelastic and damage parameters used in the radial dilatation of an idealized artery [44, 46].

Type	Part	Description	Symbol	Values	Units
Hyperelastic	Medial layer	Shear modulus	$\mu_e$	<i>uncertain</i>	kPa
		Bulk modulus	$\kappa_e$	5	MPa
		Material parameter	$k_1$	5.15	MPa
		Material parameter	$k_2$	8.64	-
		Dispersion parameter	$\kappa_0$	0.24	-
		Fiber orientation angle	$\theta$	$\pm 38.8$	deg
	Plaque	Shear modulus	$\mu_p$	20	kPa
		Bulk modulus	$\kappa_p$	34	kPa
	Balloon	Shear modulus	$\mu_b$	10	kPa
		Bulk modulus	$\kappa_b$	10	kPa
Damage	Medial layer	Damage threshold	$r_1$	1.0	kPa
		Internal length scales	$c_d$	<i>uncertain</i>	$\text{kPa}^{-1} \cdot \text{mm}^2$
		Penalty parameter	$\beta_d$	10	$\text{kPa}^{-1}$
		(Non-)local switch	$\gamma_d$	1.0	—



Table 6: The uncertain input parameters for different cases.

Case	$\mu_e$ (kPa)			$c_d$ (kPa <sup>-1</sup> · mm <sup>2</sup> )		
	Distribution	Mean	Standard Deviation	Distribution	Mean	Standard Deviation
1	$B(2.98, 8.72)$	25.58	5.03	0.01 (deterministic)		
2	25.58 (deterministic)			$B(4, 4)$	0.01	0.0017
3	$B(2.98, 8.72)$	25.58	5.031	$B(4, 4)$	0.01	0.0017

Table 7: The comparison of the computational cost between using the Monte Carlo method with the direct FEM and the Monte Carlo method with the surrogate model.

Monte Carlo method with the direct FEM (Estimated $t_1$ )	Monte Carlo method with the surrogate model			$t_2/t_1$
	Training the surrogate model	Probability analysis	Total time ( $t_2$ )	
230.09 days	19422 sec	35.43 sec	19457.43 sec	0.09%

590 **List of Figures**

591 1 Qualitative simulation based on the damage model used in this paper and the  
592 experimental stress-strain data of the abdominal aortic aneurysm in Raghavan  
593 et al. [38]. Material parameters are chosen as  $\mu_e = 0.3$  MPa,  $\kappa_0 = 100$  MPa,  
594  $k_1 = 0.22$  MPa,  $k_2 = 1.20$ ,  $\theta = 50$  deg,  $\varkappa = 0.18$ ,  $r_1 = 0.05$  MPa. . . . . 28

595 2 An example for calculating the PoF, in which the damage function is assumed  
596 to obey a beta distribution as  $f(d) \sim B(4, 4)$  within the interval  $(0, 1]$  and  
597 the maximum damage is set to  $f(d)^{max} = 0.5$ . . . . . 29

598 3 Reference model for an open-hole plate. (a) Geometric, dimension and bound-  
599 ary conditions; and (b) FEM mesh. . . . . 30

600 4 The contours of the damage function  $f(d)$  for three different shear modulus  
601  $\mu_0$  when  $\lambda_x = 0.1$ . (a)  $\mu_0 = 0.05$  MPa (b)  $\mu_0 = 0.1$  MPa and (c)  $\mu_0 = 0.15$  MPa. 31

602 5 The average Cauchy stress in  $x$ -direction  $\sigma_x$  of the right-hand side for three  
603 different shear modulus  $\mu_0$  when  $\lambda_x = 0.1$ . . . . . 32

604 6 The contours of the damage function  $f(d)$  for three different internal length  
605 scales  $c_d$  when  $\lambda_x = 0.1$ . (a)  $c_d = 0.5$  MPa $^{-1} \cdot$  mm $^2$  (b)  $c_d = 1$  MPa $^{-1} \cdot$  mm $^2$   
606 and (c)  $c_d = 5$  MPa $^{-1} \cdot$  mm $^2$ . . . . . 33

607 7 The average Cauchy stress in  $x$ -direction  $\sigma_x$  of the right-hand side for three  
608 different internal length scales  $c_d$  when  $\lambda_x = 0.1$ . . . . . 34

609 8 The comparison of the surrogate model with the SGCM and FEM. (a) The  
610 Cauchy stress in direction  $x$  at Node 1 for Case 2, (b) The damage function  
611  $f(d)$  at Node 1 for Case 2, (c) The Cauchy stress in direction  $x$  at Node 1 for  
612 Case 3, and (d) The damage function  $f(d)$  at Node 1 for Case 3. . . . . 35

613 9 PDFs of the damage function  $f(d)$  for different situations. (a) PDF of the  
614 damage function  $f(d)$  at Node 3 for Cases 1-3. (b) PDF of the damage  
615 function  $f(d)$  at different locations for Case 3. (c) PDF of the damage function  
616  $f(d)$  at Node 3 for Cases 3-5. (d) PDF of the damage function  $f(d)$  at Node  
617 3 for Case 6 and Case 7. . . . . 36

618 10 Reference model in the radial dilatation of an idealized artery. (a) Geometry,  
619 dimensions and boundary conditions; and (b) FEM mesh. . . . . 37

620 11 The comparison of the results obtained by surrogate model with the SGCM  
621 and FEM. (a) The damage function  $f(d)$  at Node 1 for Case 1, (b) The  
622 damage function  $f(d)$  at Node 1 for Case 2, and (c) The damage function  
623  $f(d)$  at Node 1 for Case 3. . . . . 38

624 12 The contours of the damage function  $f(d)$  obtained by the surrogate model  
625 with the SGCM and FEM for different shear modulus and the internal length  
626 scales when  $\lambda = 100\%$ . (a)  $\mu_e = 15$  kPa,  $c_d = 0.01$  kPa $^{-1} \cdot$  mm $^2$ , (b)  $\mu_e =$   
627  $55$  kPa,  $c_d = 0.01$  kPa $^{-1} \cdot$  mm $^2$ , (c)  $\mu_e = 35$  kPa,  $c_d = 0.005$  kPa $^{-1} \cdot$  mm $^2$ , and  
628 (d)  $\mu_e = 35$  kPa,  $c_d = 0.015$  kPa $^{-1} \cdot$  mm $^2$  . . . . . 39

629 13 The PDF of the damage function  $f(d)$  for different cases at different locations  
630 when  $\lambda = 100\%$ . . . . . 40

631 14 The PDFs of the damage function  $f(d)$  for different situations at Node 1. (a)  
632 The PDFs of the damage function  $f(d)$  for different internal length scales  $c_d$   
633 when  $\lambda = 100\%$ , and (b) The PDFs of the damage function  $f(d)$  for different  $\lambda$ . 41

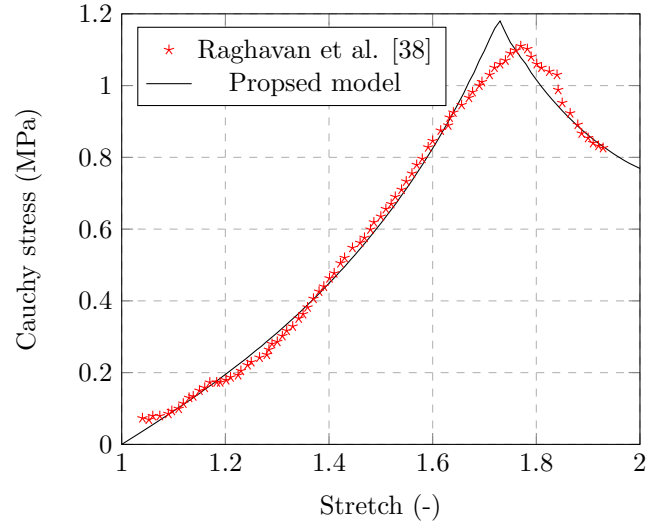


Figure 1: Qualitative simulation based on the damage model used in this paper and the experimental stress-strain data of the abdominal aortic aneurysm in Raghavan et al. [38]. Material parameters are chosen as  $\mu_e = 0.3$  MPa,  $\kappa_0 = 100$  MPa,  $k_1 = 0.22$  MPa,  $k_2 = 1.20$ ,  $\theta = 50$  deg,  $\varkappa = 0.18$ ,  $r_1 = 0.05$  MPa.

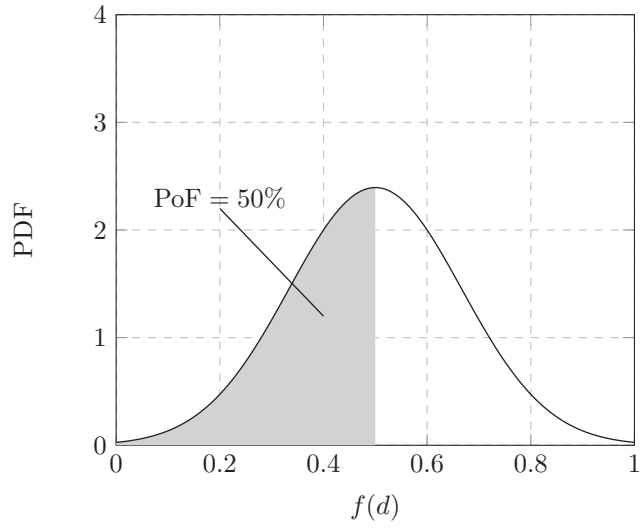


Figure 2: An example for calculating the PoF, in which the damage function is assumed to obey a beta distribution as  $f(d) \sim B(4, 4)$  within the interval  $(0, 1]$  and the maximum damage is set to  $f(d)^{max} = 0.5$ .

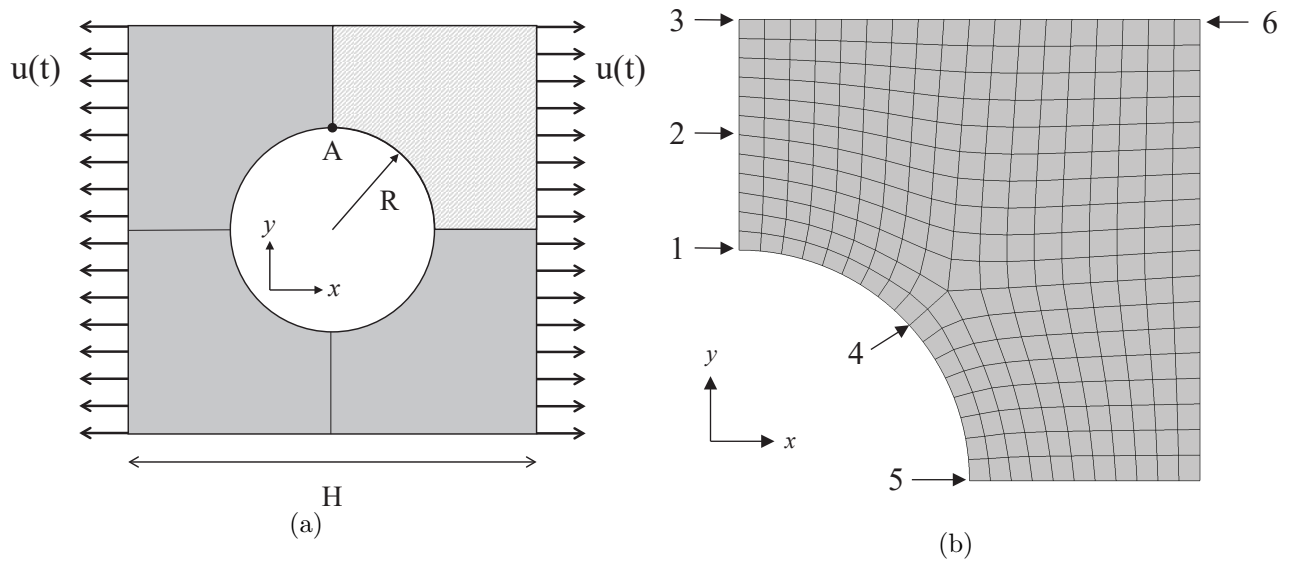


Figure 3: Reference model for an open-hole plate. (a) Geometric, dimension and boundary conditions; and (b) FEM mesh.

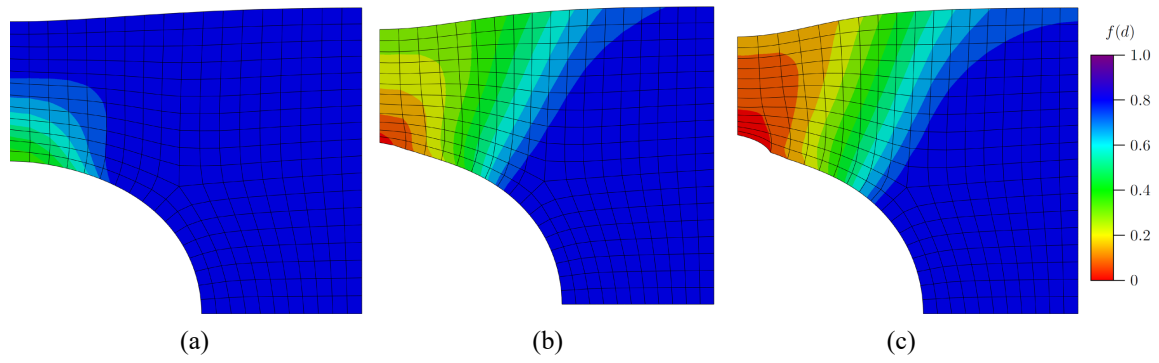


Figure 4: The contours of the damage function  $f(d)$  for three different shear modulus  $\mu_0$  when  $\lambda_x = 0.1$ .  
 (a)  $\mu_0 = 0.05$  MPa (b)  $\mu_0 = 0.1$  MPa and (c)  $\mu_0 = 0.15$  MPa.



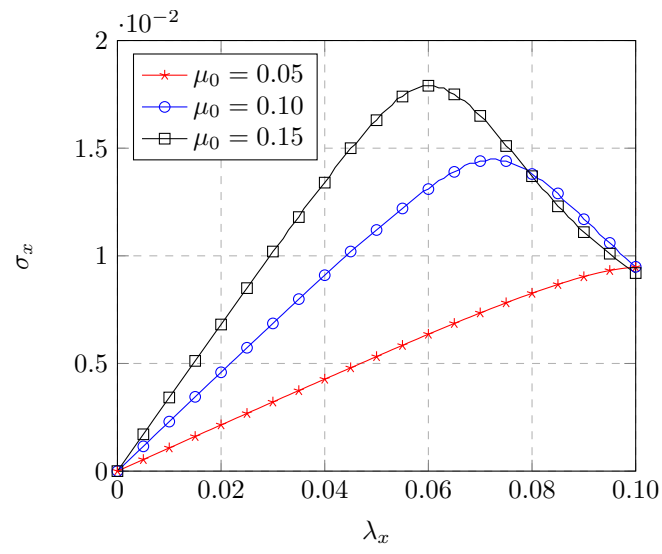


Figure 5: The average Cauchy stress in  $x$ -direction  $\sigma_x$  of the right-hand side for three different shear modulus  $\mu_0$  when  $\lambda_x = 0.1$ .

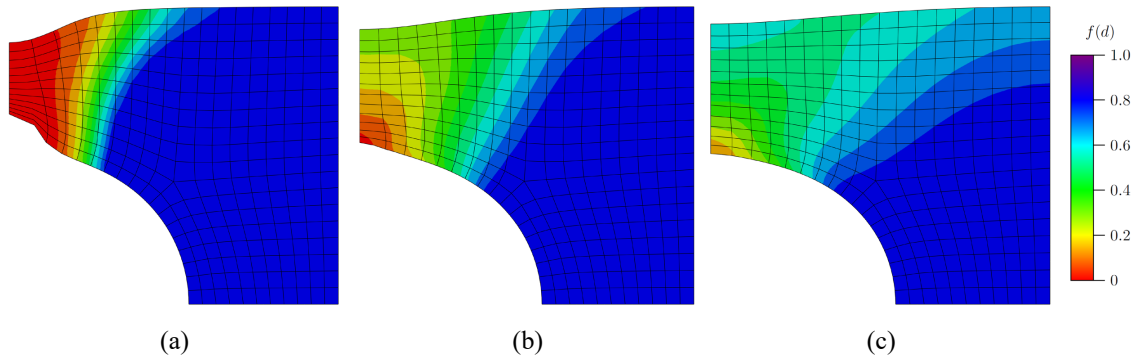


Figure 6: The contours of the damage function  $f(d)$  for three different internal length scales  $c_d$  when  $\lambda_x = 0.1$ . (a)  $c_d = 0.5 \text{ MPa}^{-1} \cdot \text{mm}^2$  (b)  $c_d = 1 \text{ MPa}^{-1} \cdot \text{mm}^2$  and (c)  $c_d = 5 \text{ MPa}^{-1} \cdot \text{mm}^2$ .

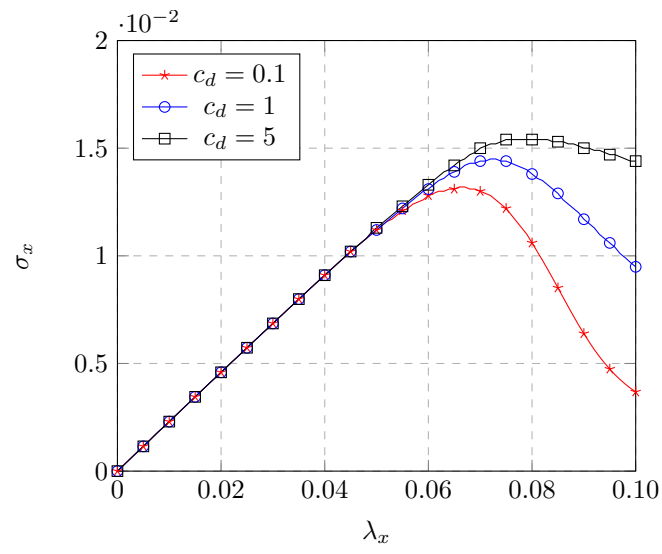


Figure 7: The average Cauchy stress in  $x$ -direction  $\sigma_x$  of the right-hand side for three different internal length scales  $c_d$  when  $\lambda_x = 0.1$ .

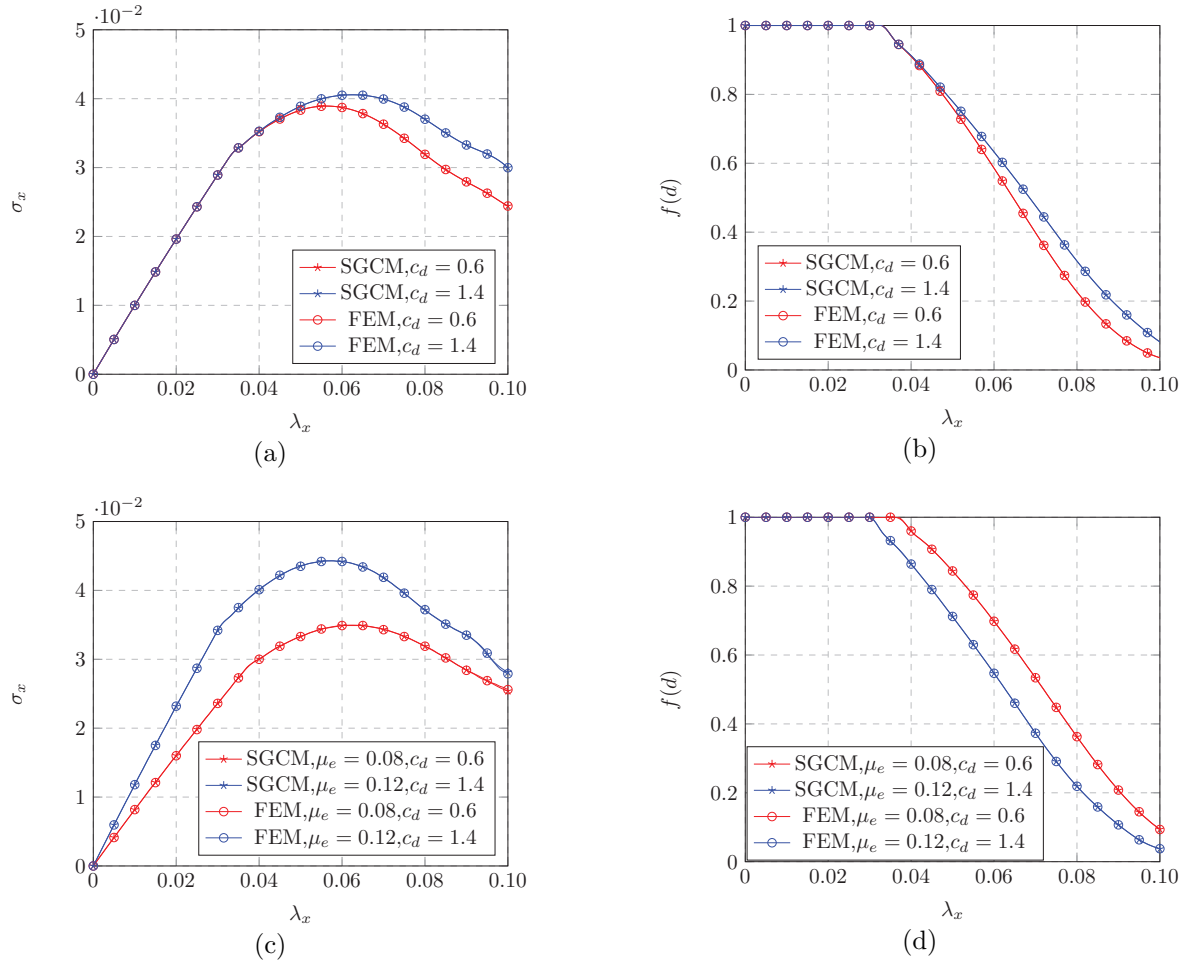


Figure 8: The comparison of the surrogate model with the SGCM and FEM. (a) The Cauchy stress in direction  $x$  at Node 1 for Case 2, (b) The damage function  $f(d)$  at Node 1 for Case 2, (c) The Cauchy stress in direction  $x$  at Node 1 for Case 3, and (d) The damage function  $f(d)$  at Node 1 for Case 3.

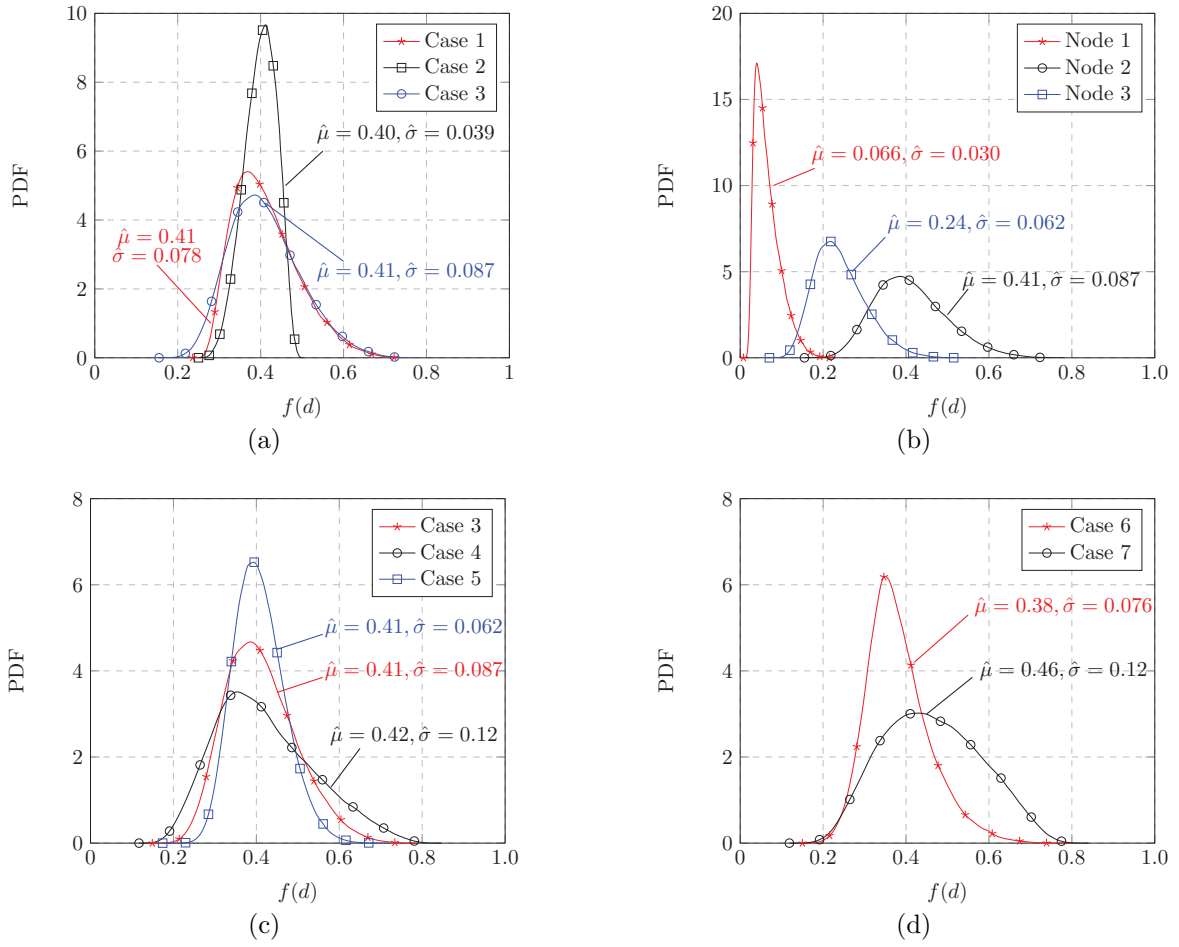


Figure 9: PDFs of the damage function  $f(d)$  for different situations. (a) PDF of the damage function  $f(d)$  at Node 3 for Cases 1-3. (b) PDF of the damage function  $f(d)$  at different locations for Case 3. (c) PDF of the damage function  $f(d)$  at Node 3 for Cases 3-5. (d) PDF of the damage function  $f(d)$  at Node 3 for Case 6 and Case 7.

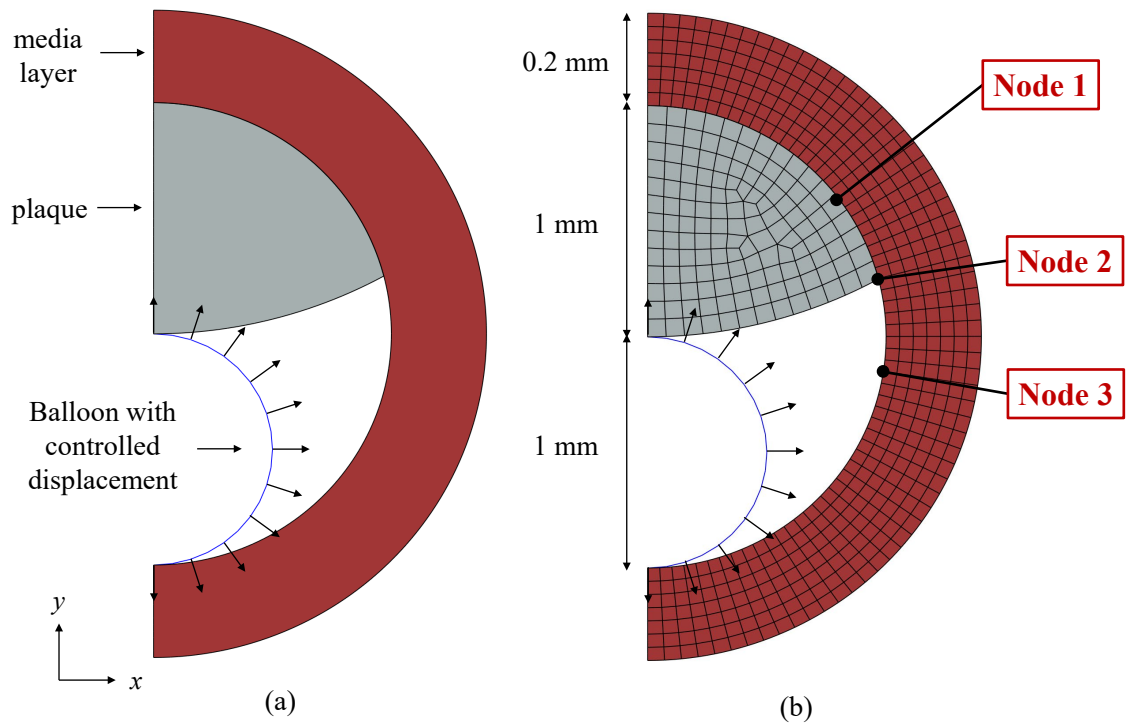


Figure 10: Reference model in the radial dilatation of an idealized artery. (a) Geometry, dimensions and boundary conditions; and (b) FEM mesh.

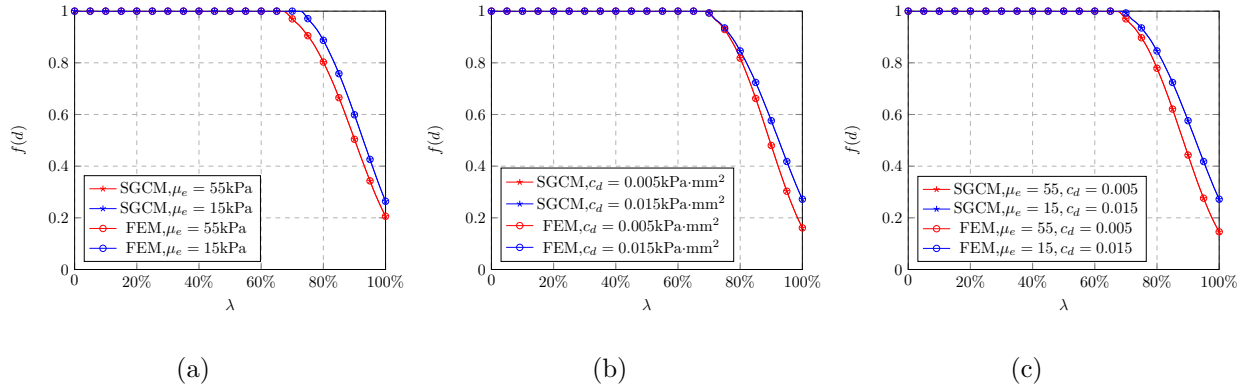


Figure 11: The comparison of the results obtained by surrogate model with the SGCM and FEM. (a) The damage function  $f(d)$  at Node 1 for Case 1, (b) The damage function  $f(d)$  at Node 1 for Case 2, and (c) The damage function  $f(d)$  at Node 1 for Case 3.

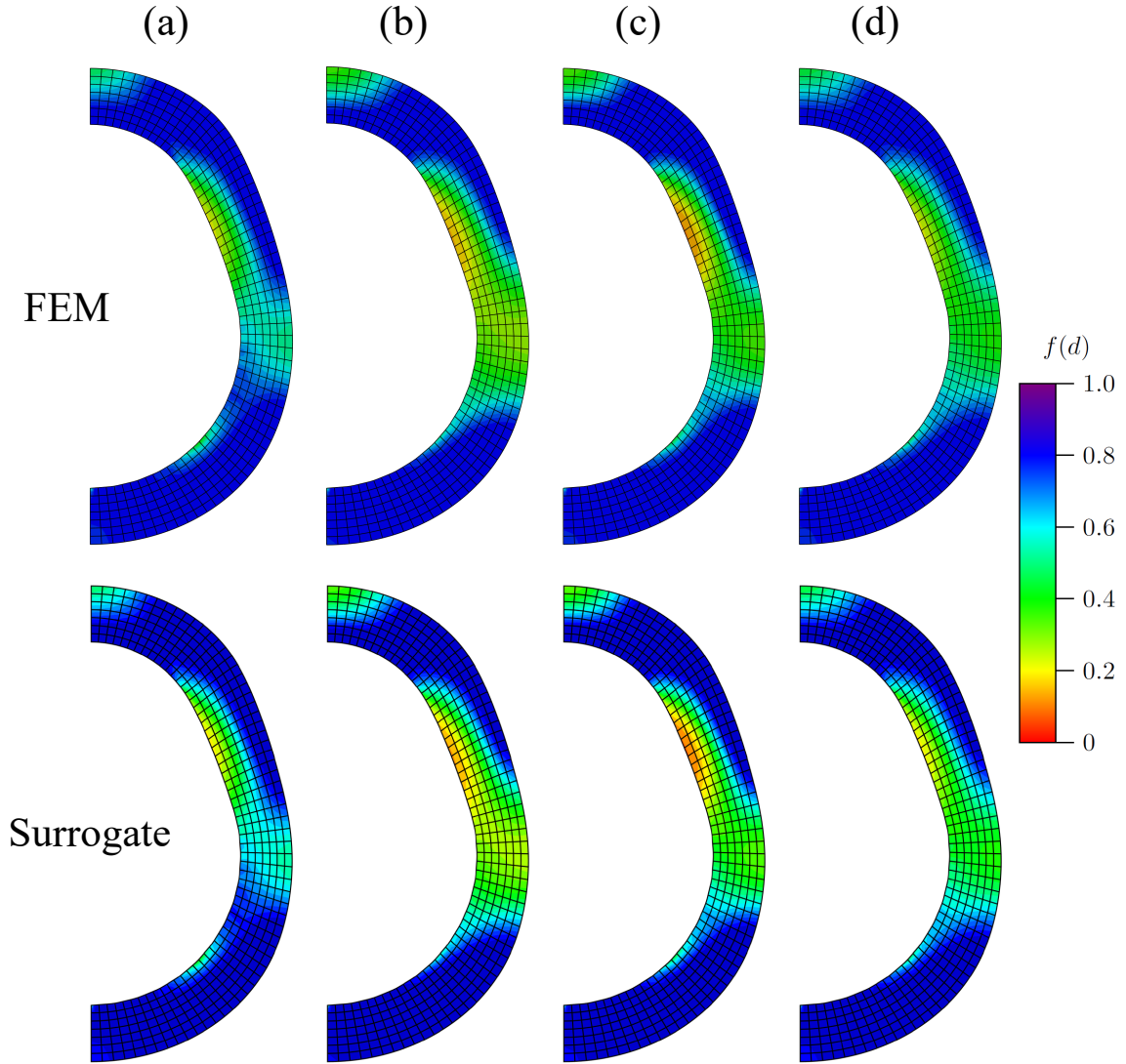


Figure 12: The contours of the damage function  $f(d)$  obtained by the surrogate model with the SGCM and FEM for different shear modulus and the internal length scales when  $\lambda = 100\%$ . (a)  $\mu_e = 15$  kPa,  $c_d = 0.01$  kPa $^{-1} \cdot \text{mm}^2$ , (b)  $\mu_e = 55$  kPa,  $c_d = 0.01$  kPa $^{-1} \cdot \text{mm}^2$ , (c)  $\mu_e = 35$  kPa,  $c_d = 0.005$  kPa $^{-1} \cdot \text{mm}^2$ , and (d)  $\mu_e = 35$  kPa,  $c_d = 0.015$  kPa $^{-1} \cdot \text{mm}^2$



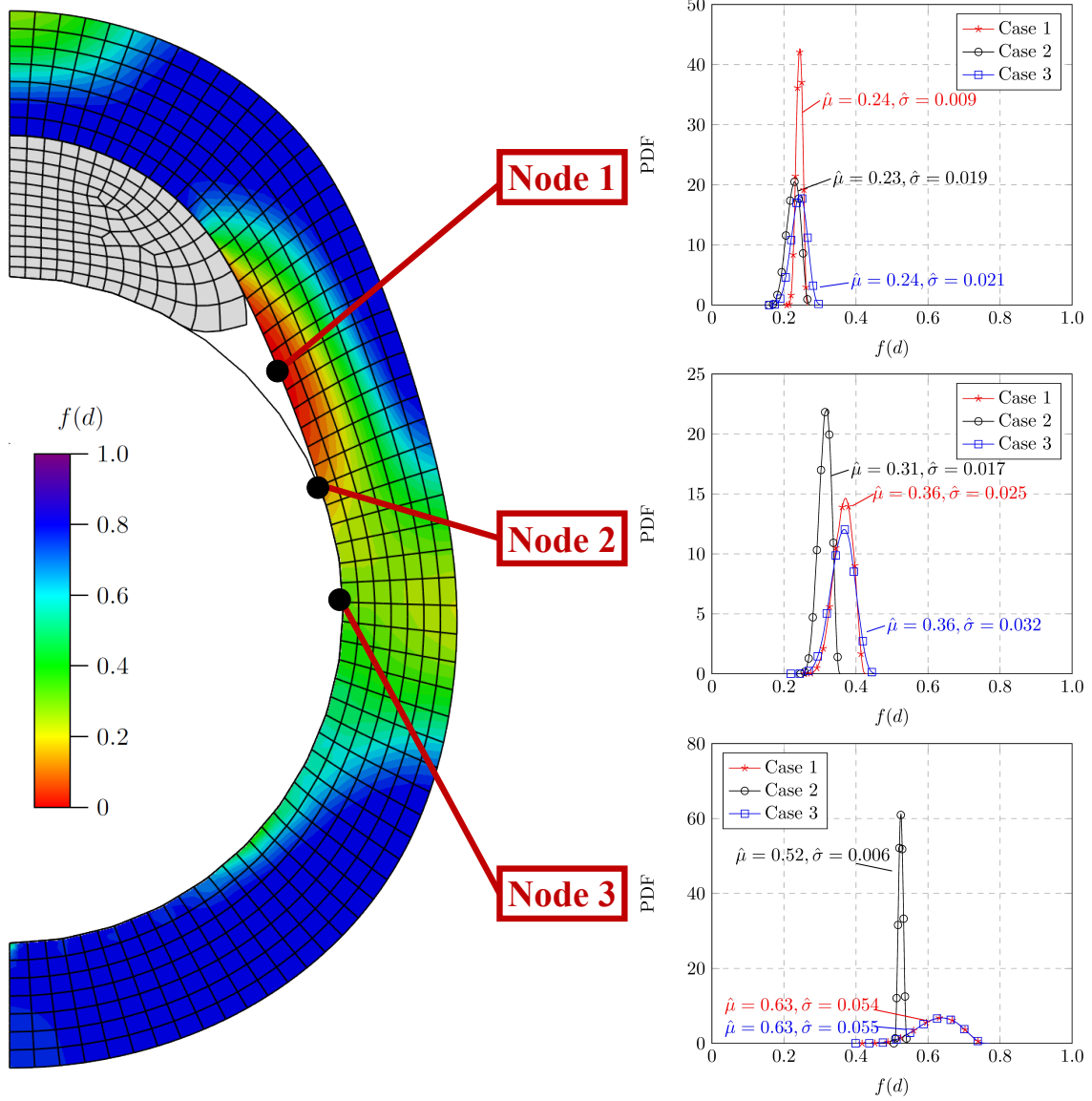


Figure 13: The PDF of the damage function  $f(d)$  for different cases at different locations when  $\lambda = 100\%$ .

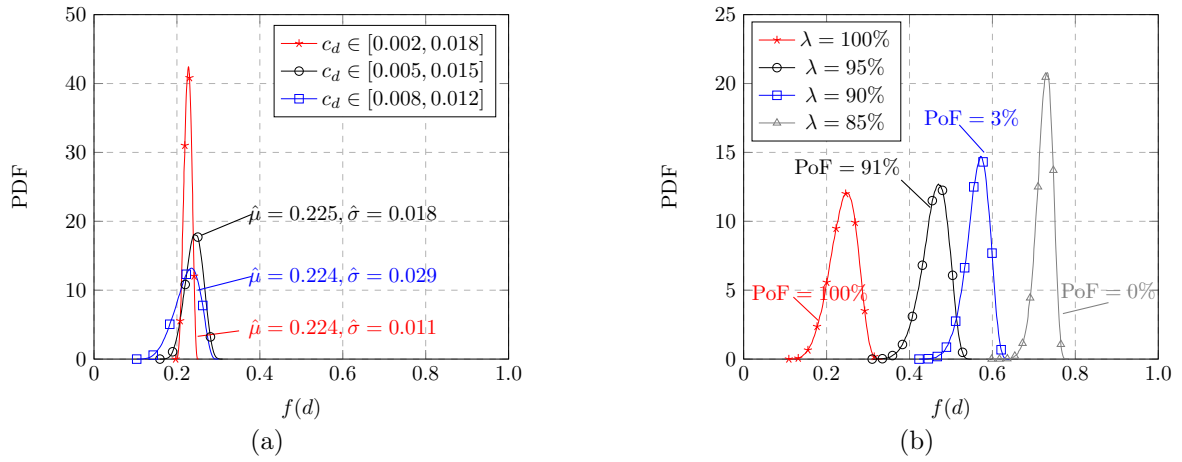


Figure 14: The PDFs of the damage function  $f(d)$  for different situations at Node 1. (a) The PDFs of the damage function  $f(d)$  for different internal length scales  $c_d$  when  $\lambda = 100\%$ , and (b) The PDFs of the damage function  $f(d)$  for different  $\lambda$ .